CHALMERS
UNIVERSITY OF TECHNOLOGY

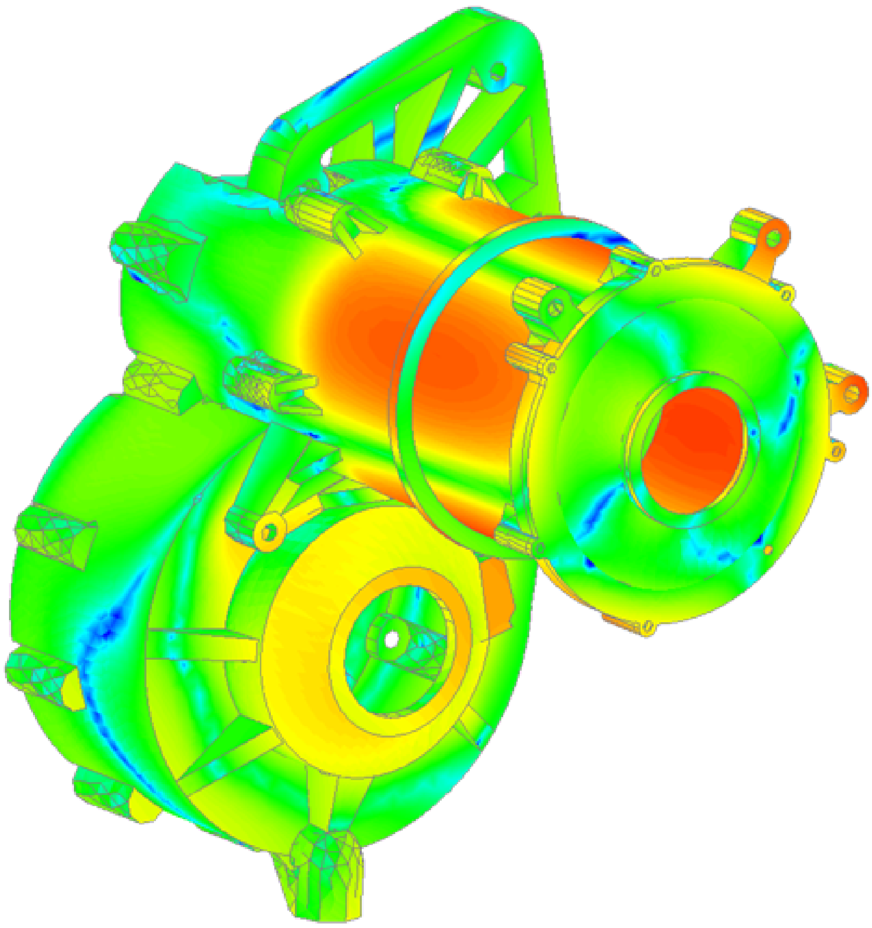

Analysis of Force and Torque Harmonic Spectrum in an Induction Machine for Automotive NVH Purposes

Master's thesis in Electric Power Engineering

INIGO GARCIA DE MADINABEITIA

Department of Energy and Environment
CHALMERS UNIVERSITY OF TECHNOLOGY
Gothenburg, Sweden, 2016

Master's thesis 2016

Analysis of Force and Torque Harmonic Spectrum in an Induction Machine for Automotive NVH Purposes

INIGO GARCIA DE MADINABEITIA

Department of Energy and Environment
Division of Electric Power Engineering
Chalmers University of Technology
Gothenburg, Sweden 2016

Analysis of Force and Torque Harmonic Spectrum in an Induction Machine for Automotive NVH Purposes
INIGO GARCIA DE MADINABEITIA

Supervisor: Mehdi Mehrgou, AVL List GmbH.
Examiner: Sonja Lundmark, Energy and Environment

Master's Thesis 2016
Department of Energy and Environment
Division of Electric Power Engineering
Chalmers University of Technology
SE-412 96 Gothenburg
Telephone +46 31 772 1000

Cover: Combined excitation normal surface velocity levels at $6045 rpm$ $1209 Hz$

Typeset in LaTeX
Gothenburg, Sweden 2016

Analysis of Force and Torque Harmonic Spectrum in an Induction Machine for Automotive NVH Purposes
INIGO GARCIA DE MADINABEITIA
Department of Energy and Environment
Chalmers University of Technology

Abstract

Currently, hybrid and fully electric vehicles are being developed in a great variety regarding topology, power and range. This requires a new methodology for *NVH* (Noise Vibration and Harshness) evaluation of potential problems early in the design phase. This methodology requires reliable simulation approaches for hybrid and electric drivetrains, concerning the whole automobile, and not limited to the electric machine. One of the main *NVH* sources is the electric drive, as the excitations in the electric motor, caused by the electromagnetic forces, excite its housing and that of the drivetrain, causing a structure-borne vibration. Torque ripple generates excitations in the shaft and gearbox, which are then transmitted to the whole drivetrain housing. It is seen that a low-torque-ripple design aim might not be enough for reducing the *NVH* issues, and specially radiated noise, in a fully electric or hybrid drivetrain, since Maxwell forces experienced by the stator can be present in frequencies where there is no torque harmonic. Since analytic models cannot represent accurately the non-linearity of the magnetic field and the detailed design of the stator and rotor geometries, the *FEM* (Finite Element Method) simulations are unavoidable to study the electrical motors in detail. A *FEM* tool is used in this project to design and assess the performance of an induction machine, focusing on the effect that driving profile and control unit cause on the electric drive, magnetic field and forces in the system for different driving conditions. The produced forces are evaluated to assess the noise and vibration in the system. It is seen that *FEM* results correlate with what theory predicts, as force harmonic orders are 0, 2 and $n \pm 1$, where n is any magnetic flux density harmonic. The center tooth point only experiences radial forces, whereas the corner points have tangential stress as well, due to saturation. An example of $15\mu m$ dynamic eccentricity illustrates alterations force and torque harmonic magnitudes due to shaft assembly eccentricity or shaft bending caused by bearing clearance and/or stiffer gear contact vibration.

Keywords: induction, motor. drivetrain, NVH, automotive, electric, vehicle, mobility, noise.

Acknowledgements

I would like to dedicate a few lines to every person who has contributed, willing or unwillingly, to my academic and personal life, for I shall not have achieved this goal without you.

The man to blame for each and every good thing I have ever attained is *Pedro García de Madinabeitia*. I have not found any word in the dictionary which can describe what I think of you, so I will just say *thank you*. To maintain this line, I would like to ask my mother and brother for forgiveness, as they have stood many of our crazy, foolish and absurd ideas for very long.

I would like to thank the *AVL DAD* and *DAM* teams, and especially *Mehdi Mehrgou* for encouraging me to give my best for such a long period, for your valuable insight on *NVH* and for supervising my work, even when projects do not leave room to think clearly.

I would not like to finish these lines without thanking *Sonja Lundmark* for being my academic supervisor and examiner. This report would look much more untidy without your sugestions.

Inigo Garcia de Madinabeitia, Gothenburg, August 2016

"Seek simplicity and distrust it"
Alfred North Whitehead

"The truth is rarely pure and never simple"
Oscar Wilde

"Name the greatest of all inventors. Accident"
Mark Twain

Contents

1

Introduction

1.1 Background

Sealed on the 12^{th} December 2015 and signed by 177 countries on the 22^{nd} April 2016, the *Paris Agreement* is thought to be a historic turning point in the race towards the reduction of human-caused climate change. The *Kyoto Protocol* and *Copenhagen Accord* are other examples of the concern about the implication of climate change on the lives on human life in every continent.

Road transportation is held accountant for 71% of the total transport CO_2 emissions in the European Union [1]. Electrification of transport, especially light duty vehicles, has a very significant potential of greenhouse gas emissions [2].

Most automotive *OEM*s are working in in this direction, with an increasing number of electric and hybrid models in their catalog, which are more ambitious and with improved performances in every redesign iteration. It is shown in figure 1.1 that manufacturers have different ideas about their targeted electric vehicle markets, but most of the cars are found in the 1300-1700kg and 80-110kW range. The arrow illustrates that the power-mass relation seems to follow a non-linear trend, with more powerful vehicles in the high weight area.

All electric vehicles have one thing in common: they are propelled by electric drives, formed by electrical machines and power electronics. An electrical machine is a device which transforms mechanical energy into magnetic energy and further into electrical energy or *vice versa*. If the energy flow is from mechanical to electrical, the machine has a generator behavior, and if the flow is the opposite, motor [3]. If the machine absorbs or generates Alternate Current, it is called AC machine, whereas it is named DC machine if its performance is based on Direct Current. AC machines can be divided in two categories, synchronous and asynchronous, depending on the operating speed. Inside the synchronous machine category, there are many different designs, such as Synchronous Reluctance Machines, Switched Reluctance Machines (*SRM*) and Permanent Magnet Synchronous Machines (*PMSM*). On the other hand, the asynchronous machine, is also known as Induction Machine (*IM*), due to the fact that it needs a slip to work. This study will be based on the Induction Machine and its relation with Noise, Vibration and Harshness (*NVH*).

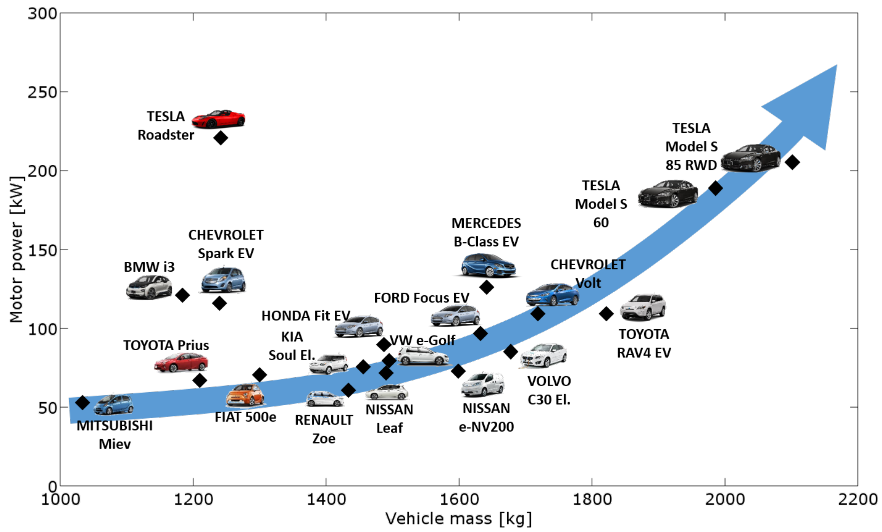

Figure 1.1: Power and mass relation in the existing electric vehicles in the market (June 2016)

Electric motors have existed since a very long time ago, but more and more topologies are appearing in the last few years. These topologies are very application-focused, efficient and optimized. However, automotive applications require a big working range regarding speed, supply frequency and torque capability. The most suited motor types for this application are the *SRM*, *PMSM* and *IM* [4]. Figure 1.2 shows a comparison between the three, where the *IM* is believed to have the best overall score in the automotive mass-produced scale market, where noise, cost and fault tolerance are essential [5].

Category \ Motor Type	PMSM	Induction	SRM
Power/Torque Density	High	Medium	Medium
Efficiency	High	Medium	Low
Torque ripple	Low	Low	High
Noise	Medium	Low	High
Motor cost	High	Medium	Low
Controller cost	Medium	Medium	High
Fault tolerance	Poor	Excellent	Excellent
Winding locations	Stator	Stator and rotor	Stator
Reliability	Medium	High	High

Figure 1.2: Comparison between *PMSM*, *IM* and *SRM* optimality for automotive applications

Moreover, the use of *IM* in *Tesla Motors Model S* , *Roadster*, *Toyota RAV4 EV* and *Mercedes B-Class Electric Drive* proves that this technology is very well suited for high-end and high performance sport cars, as well as for *SUV*s and compact city cars. A key factor, price, may make one of these motor types win the battle in the long term in case there is no breakthrough of a new technology better suited for this application.

1.2 Aim

The aim of this report is to analyze the harmonic spectrum of an induction machine and how these harmonics affect the NVH of the drivetrain in an automotive application.

1.3 Scope

PWM losses in the inverter will not be adressed. Although, iron loss increase due to high-order harmonics is accounted for.

Furthermore, this thesis will not analyze magnetostriction. The interested reader should instead refer to the work of *Le Besnerais* [6] or *Belahcen* [7].

The cage end-rings and coil connections will only be considered as additional resistance in the cage and not as elements in the *FEM* models.

The effects of the drivetrain NVH dynamics from section 3.3 will not be considered when evaluating eccentricity, but only when evaluating the torque ripple in the system.

Base frequency for harmonic order detection is defined as the number of pole pairs multiplied by the rotation frequency, *i.e.* the electrical supply frequency multiplied by one minus the slip, expressed as per unit value.

Harmonic orders will only be considered in the 0-50th range. Higher orders are assumed not to be hazardous due to the lower magnitude of higher frequency oscillations and due to the increase of mechanical damping as frequency increases.

Transient effects will not be considered in the frequency domain analysis, but only in the driving cycle and speed run up simulations. The reader can find information about transient harmonics in *Tu et al.* paper [8].

There will not be optimization iterations in the speed run up and gear ratio comparison.

The driving cycle analysis is performed under the assumption that the battery can always be recharged, and that up to 50% of the rated machine power can be recovered.

2

Induction Machine Theory

2.1 Introduction

If there is a mismatch between supply frequency and rotation frequency, there will be a slip s, defined as

$$s = \frac{\omega_1 - \omega_r}{\omega_1} \tag{2.1}$$

where ω_1 is the frequency of the current in the stator windings and ω_r the rotation speed of the machine. If the slip is non-zero, the machine is said to be asynchronous, and, if both frequencies are equal, *i.e.* zero slip, synchronous [9].

The major advantages of the induction machine are cost and reliability. It is much less costly than a Permanent Magnet Synchronous Machine (*PMSM*), since there is no need for expensive materials, such as rare earth magnets. Another advantage against novel types of machines is that the *IM* has been studied for a long time, so the know-how is widely available, and, thus, developments can be made fastly and in a collaborative manner. Fault detection has already been studied and can be easily diagnosed [10]. Although induction machines are traditionally used as fixed speed drive, the appearance of Variable Frequency Drives (*VFD*) makes the *IM* work in a wide range of speeds, maximizing performance and energy efficiency.

The need for high speed operation implies various challenges in the design and operation of electric drives, such as high-speed losses and increased need of reactive power supply [11,12]. These need to be taken into account when designing automotive powertrains involving electric drives.

2.2 Geometry

Motors can have various shapes and sizes, but all of them have the same components: stator, rotor, windings, cage and shaft. The shaft serves as interface with the mechanical system, whereas the stator windings serve as interface for the electric system [3]. The 2D motor model represented in figure 2.1 is a squirrel-caged rotor, with 38 aluminium bars and 48 stator teeth, which result in 2 pole pairs. The *3D* model can be seen in figure 2.2.

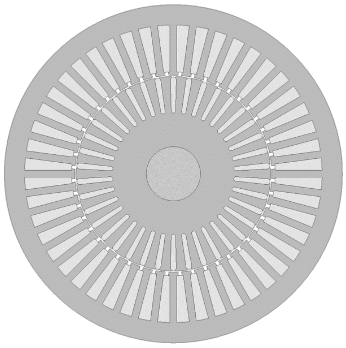

Figure 2.1: Induction motor geometry with 48 stator teeth and 38 rotor bars

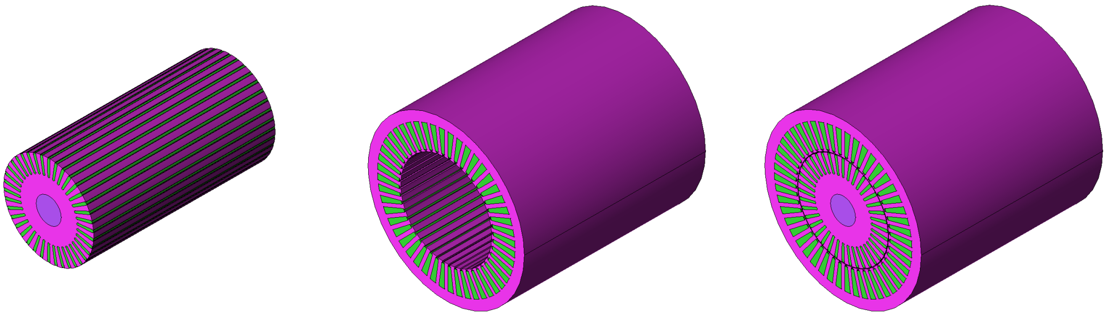

(a) Rotor, bars and shaft **(b)** Stator and windings **(c)** Full machine

Figure 2.2: Separate *3D* views of the induction machine components, excluding end-rings and coil connections

The motor can be evaluated as a *2D* or *3D* model, the latter being more computationally consuming but able to include elements such as end-rings, winding ends and features like rotor skewing or tilted axle. As a result, *3D* analysis is also performed to compare and decide if the additional computational effort is compensated with increased accuracy.

The detailed geometries of rotor and stator play a crucial role in the harmonic spectrum evaluation of forces and torque, since saturation is closely related to the surface which the magnetic flux crosses.

2.3 Magnetic flux

The principle of electrical machines is based on the electromagnetic force, which is accountable for the rotation and some harmonics.

2.3.1 Maxwell forces

The main electromagnetic source of noise from an induction machine is due to the so called Maxwell forces. These make the stator vibrate, and this vibration is ultimately transmitted as noise by means of the surrounding air to the perceivers. The electromagnetic force acting on the stator, F, is defined as

$$F = \oint_S \sigma \mathrm{d}S \tag{2.2}$$

where σ is the Maxwell stress tensor and S is the surrounding surface of the stator core. As the flux is concentrated in the rotor-stator gap, it can be considered that the total force is equal to the rotor-stator gap surface force, and discriminate the stator outer surface. *Kloos* [13] defined the Maxwell stress tensors as σ_n and σ_t in equations

$$\sigma_n = \frac{1}{2}\mu_i(H_n^2 - H_t^2) - \frac{1}{2}\mu_0(H_n^{'2} - H_t^{'2}) \tag{2.3}$$

$$\sigma_t = \mu_i H_n H_t - \mu_0 H_n^{'2} H_t^{'2} \tag{2.4}$$

where μ_i is the magnetic permeability of the stator core, H stands for magnetic field intensity in the core and $H^{'}$ for the magnetic field intensity in the air gap.

As the laws of flux continuity state [14], $H_t = H_t^{'}$ for no surface currents on the boundary, and $B_n = B_n^{'}$, meaning that the stress tensors can be simplified to [6]:

$$\sigma_n = \frac{1}{2}(\mu_i \mu_0 H_t^{'2} + B_n^{'2})(\frac{1}{\mu_i} - \frac{1}{\mu_0}) \tag{2.5}$$

$$\sigma_t = 0 \tag{2.6}$$

Therefore, Maxwell stress in the surface limiting stator and air-gap is a normal stress, radial direction. It is important to say that this radial direction of the stress has nothing to do with the incidence angle of the magnetic flux lines, but it is independent from that parameter and the result only highlights the application of the flux and field continuity laws. Further simplification can be performed in the Maxwell stress equation, by assuming the radial flux is much greater than the tangential component and that the material is not saturated [6]. Then,

$$\sigma_n \approx \frac{B_n^{'2}}{2\mu_0} \tag{2.7}$$

From this, the force harmonics can be predicted, as Maxwell forces are a function of B^2. The harmonic spectrum is modified, even in a perfect sinusoidal magnetic flux density waveform case, due to

$$2\cos^2(x) = 1 + \cos(2x) \tag{2.8}$$

Thus, $2nd$ harmonic will always exist in the forces applied on the stator teeth, even in a perfect sinusoidal input case. This can be seen in figures 2.3 and 2.4, where the

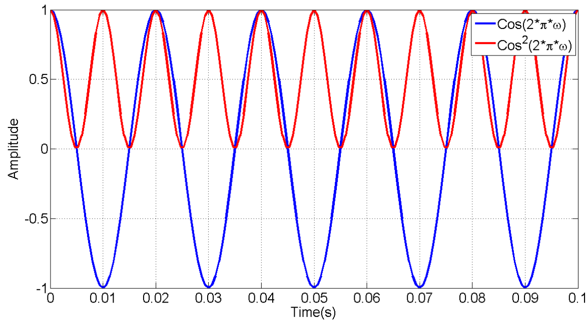

Figure 2.3: Time waveforms $cos(2\pi\omega)$ and $cos^2(2\pi\omega)$

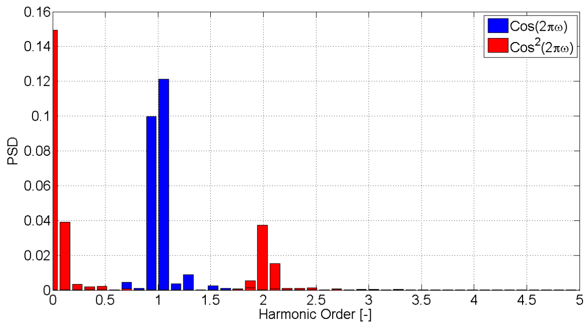

Figure 2.4: Harmonic spectrum of $cos(2\pi\omega)$ and $cos^2(2\pi\omega)$

time waveforms and frequency components of a cosine and its squared function are computed.

Apart from this, all magnetic flux density harmonic orders are modified when squared, when $B(x)$ consists of two waveforms of order 1 and n, with coefficients a and b, respectively

$$B(x) = a \cdot cos(x) + b \cdot cos(nx) \tag{2.9}$$

$$B^2(x) = a^2cos^2(x) + b^2cos^2(nx) + 2ab \cdot cos(x)cos(nx) \tag{2.10}$$

$$B^2(x) = \frac{a^2[cos(0) + cos(2x)] + b^2[cos(0) + cos(2nx)]}{2} + ab[cos(x(n-1)) + cos(x(n+1))] \tag{2.11}$$

However, under the assumption that the $n - th$ harmonic magnitude, b, is smaller than the fundamental magnitude, the b^2 term becomes negligible, as $b^2 \ll a^2$, and, therefore,

$$B^2(x) = \frac{a^2[cos(0) + cos(2x)]}{2} + ab[cos(x(n-1)) + cos(x(n+1))] \tag{2.12}$$

Then, equation 2.12 shows how force orders are 0, 2 and $n \pm 1$.

2.3.2 Saturation

The saturation factor K_s from *Le Besnerais*'s work [6] is based on the flux paths across the machine, as the flux, shown in figure 2.5, goes through stator and rotor teeth twice, and through the stator and rotor bodies once. The gap is also accounted for twice. K_s is mathematically defined as

$$K_s = \frac{\mathcal{F}_g + (2\mathcal{F}_{st} + 2\mathcal{F}_{rt} + \mathcal{F}_{sy} + \mathcal{F}_{ry})}{\mathcal{F}_g} \tag{2.13}$$

where $\mathcal{F}$ represents the magnetomotive force (MMF), and the subscripts indicate gap, g; stator teeth, st; rotor teeth, rt; stator body, sy; and rotor body, ry.

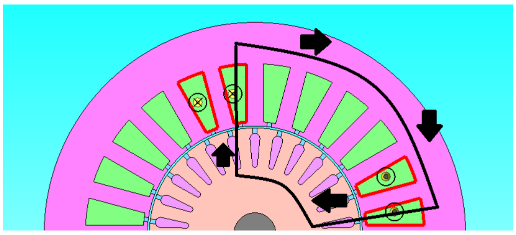

Figure 2.5: Magnetic flux path through squirrel-caged induction motor

In addition to that, it is seen in *Chitroju*'s [15] and *Petrov et al.* [16] works, for instance, that saturation causes harmonics in order

$$m_{sat} = 3p \tag{2.14}$$

which happens to be $6th$ harmonic in the case of a 2-pole-paired machine. *Plotkin et al.* [17] also found that PWM harmonics can cause the existence of the $6th$ harmonic.

2.4 Windings

Several winding setups are analyzed, as these can greatly affect the performance of the machine. Figure 2.6 shows an example of machine winding setup, with a star-connected 3-phase 1-layer coil configuration, with a pitch of 12. This different slot number and pitch setup originate variations in the *MMF*, ideally sinusoidal, see figure 2.7. This phenomenon is strongly connected to the slot harmonics, in section 2.5.1.

The equations which describe this are

$$\tau_p = \frac{\pi}{2p} \tag{2.15}$$

$$\tau_v = \frac{\tau_p}{m} \tag{2.16}$$

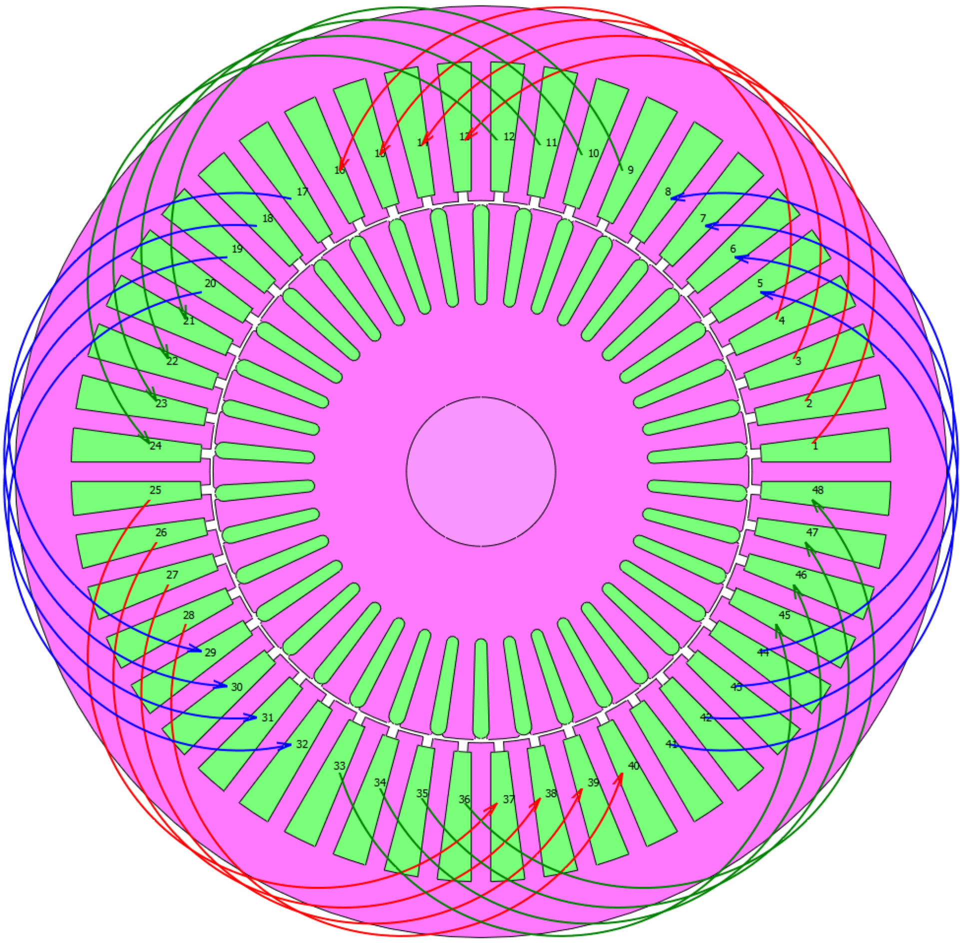

Figure 2.6: Winding diagram example in a squirrel-caged induction motor

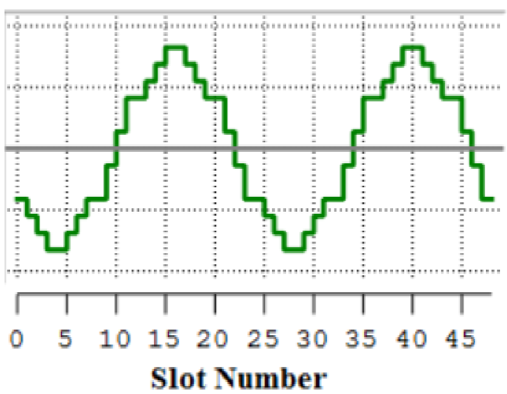

Figure 2.7: Magnetomotive force example in a 48 stator slot induction machine

$$q = \frac{Z_s}{2pm} \tag{2.17}$$

where τ_p is the pole pitch, *i.e.* the separation arc in radians of the equivalent 180 electrical degrees, p is the number of pole pairs, m is the number of phases, τ_v is the phase zone distribution, *i.e.* the pole pitch divided by the number of phases, Z_s is the total number of stator slots and q is the number of slots for each pole and phase. If q is an integer, the windings are known as integral slot windings, whereas if it is a fraction, they are called fractional slot windings [18].

The example in figure 2.6 has a $q = 4$ with $Z_s = 48$, $p = 2$ and $m = 3$, which means that the number of slots per pole and phase is 4. This can be checked by counting the different color coils in the figure. The higher q is, the more sinusoidal the *MMF* will look like [18]. In a distributed winding, a distribution factor, k_d, can be introduced to further describe the harmonics in the *MMF*. In the case where $q = 1$, $k_d = 1$, but if $q \neq 1$, $k_d < 1$. The pitch factor, k_{pv}, accounts for how wide is a pole winding in the machine. The $v - th$ component of the *MMF* wave, also known as winding factor, k_{wv}, is described mathematically in equations [18, 19]

$$k_{dv} = \frac{\sin(v\frac{\pi}{2m})}{q\sin(v\frac{\pi p}{Z_s})} \tag{2.18}$$

$$k_{pv} = \sin\left(v\frac{\pi}{2}\right) \tag{2.19}$$

$$k_{wv} = k_{dv}k_{pv} \tag{2.20}$$

Then, the peak values of the *MMF* will be [20]:

$$\hat{\mathcal{F}}_v = \frac{3\sqrt{2}}{\pi}\frac{qZ_s}{v}k_{wv}I_{rms} \tag{2.21}$$

From this, assuming there is no phase shift between harmonics, the magnetic flux density can be simplified to:

$$B(\theta, t) = \frac{\mu_0}{\delta_0}\sum_{v}^{\infty}\hat{\mathcal{F}}_v\sin(vp\theta - \omega_1 t - \varphi) \tag{2.22}$$

where δ_0 is the effective air gap length, θ is the position angle of where the magnetic flux density will be calculated and φ is the phase shift angle. δ_0 is equal to the air gap length in case of closed stator and rotor geometries. In addition, equation 2.22 can be combined with 2.7 in order to get an analytic model of the Maxwell forces created by the magnetic flux density harmonics.

2.5 Choice of rotor bars and stator teeth number

The machine generates harmonics, even with a perfectly sinusoidal input in a motor, solely by the fact of rotating [18]. As a consequence, the physical setup of the machine, *e.g.* number of stator slots, number of rotor bars and number of pole pairs, can influence the behavior of the drivetrain, by introducing harmonics in the mechanical resonance frequencies, and, thus, damaging the parts and creating noise or vibrations. The stator creates slot harmonics, section 2.5.1, and the rotor creates bar harmonics, section 2.5.2. *Pyrhönen et al.* reviewed the most advantageous and most damaging motor setups in terms of bars and teeth number [18], summarized in section 2.5.3.

2.5.1 Slot harmonics

The expected slot harmonics are defined by

$$m_{slot} = M\frac{Z_s}{p} \pm 1 \tag{2.23}$$

where m_{slot} is the order of the harmonics, M is an integer, Z_s is the number of stator slots and p the number of pole pairs [3]. The lowest, and most dangerous for *NVH*, harmonic order is obtained by using $M = 1$. Higher values of M cause, generally, lower magnitude harmonics.

However, this phenomenon is greatly affected by *MMF* harmonics from section 2.4 equation 2.21, which might amplify or reduce slot harmonics of order $\frac{Z_s}{p} \pm 1$. It is important to note that the first slot harmonics torque might be cancelled by having a skewed machine [19], see section 2.5.4 for further explanation of the skew angle.

2.5.2 Bar harmonics

Apart from the stator, the rotor also creates harmonics, and solely by the fact of rotating, as well. These phenomena are called bar harmonics. The expected bar harmonics are defined by

$$m_{bar} = M\frac{Z_r}{p} \pm 1 \tag{2.24}$$

where m_{bar} is the order of the harmonics, M is an integer, Z_r is the number of rotor bars and p the number of pole pairs [3]. Analogously to stator slot harmonics, the lowest, and most dangerous for *NVH*, harmonic order is obtained by using $M = 1$. Higher values of M cause, generally, lower magnitude harmonics.

2.5.3 Slot and bar number selection

The following equations describe the selection criteria for the optimal slot and bar setups, depending on Z_r, Z_s and p [18]:

$$Z_r < 1.25Z_s \tag{2.25}$$

$$Z_r \neq Z_s \pm 2p \tag{2.26}$$

$$Z_r \neq 2Z_s \pm 2p \tag{2.27}$$

$$Z_r \neq Z_s \pm p \tag{2.28}$$

$$Z_r \neq \frac{Z_s}{2} \pm p \tag{2.29}$$

The analysis conducted by *Pyrhönen et al.* [18] can be summarized in tables 2.1 and 2.2. As it is obvious from the tables, the ideal setups for the machine depends on its skew angle.

Table 2.1: Non-skewed stator best setups

	Z_r	
Z_s	$p = 2$	$p = 3$
36	26, 30, 42, 46	28, 34, 38, 40, 44
48	34, 38, 42, 54, 58	-
54	-	50, 52, 56, 58, 62

Table 2.2: Skewed stator best setups

	Z_r	
Z_s	$p = 2$	$p = 3$
36	24, 40, 42	42, 48, 54
48	44, 56, 60	-
54	-	48, 72

2.5.4 Skew angle

The existence of bar and slot harmonics makes the torque ripple become a problem, which can cause major *NVH* problems. A possible solution for this problem is found with a skew angle, either in the stator or the rotor. According to *Boldea* and *Nasar* [19], the skewing of the machine is highly recommended if $Z_r > Z_s$ unless magnetic wedges are used. An example of rotor skewing can be seen in figure 2.8. This reduces the torque ripple, at the cost of introducing axial forces in the stator or rotor, which have to be studied. These forces can contribute to mechanical resonances of the system, create axially directed efforts in bearings and gearbox. Furthermore, the computational cost is very dear, as the analysis becomes *3D* instead of *2D*. However, this can be solved by using a multislice approach, recommended in the *JMAG* application notes [21]. If the rotor is skewed by one stator slot pitch or more, the first stator slot harmonics is cancelled [19].

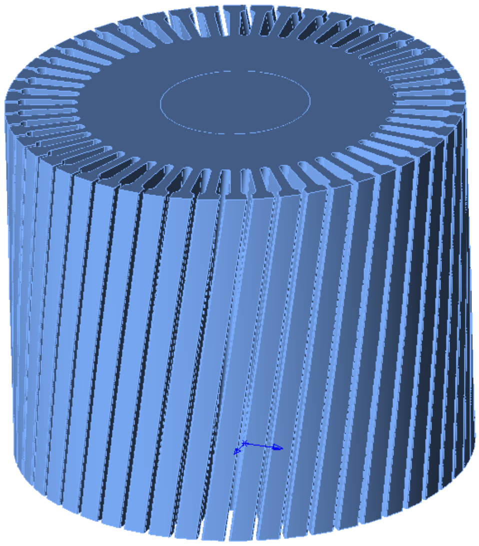

Figure 2.8: View of skewed rotor, with a skew angle of 15 degrees

2.6 Electromechanic model

There are several manners in which the machine can be described, from merely steady state resistances in the rotor and stator plus a slip-dependent resistance to highly accurate models in T, figure 2.9, or $inverse - \Gamma$ shapes, figure 2.11. Some relevant models are explained in this section.

2.6.1 Dynamic T-model for the induction machine

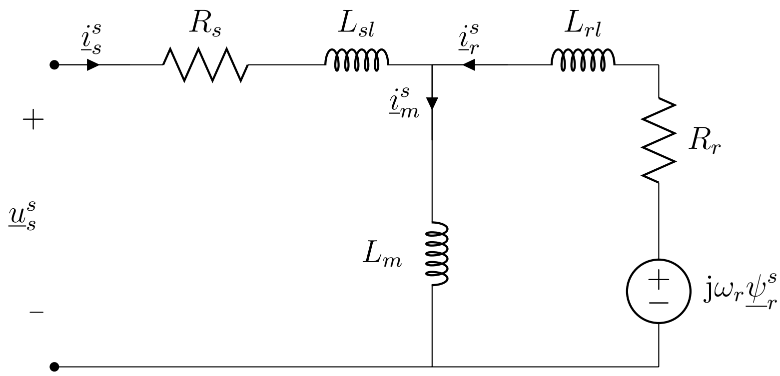

Figure 2.9: Induction machine T model circuit diagram

The following equations describe the behavior of the induction machine in an amplitude invariant arbitrary reference system [22, 23, 24]:

$$\underline{u}_s^k = R_s \underline{i}_s^k + \frac{\mathrm{d}\underline{\psi}_s^k}{\mathrm{d}t} + j\omega_k \underline{\psi}_s^k \tag{2.30}$$

$$\underline{u}_r^k = R_r \underline{i}_r^k + \frac{\mathrm{d}\underline{\psi}_r^k}{\mathrm{d}t} + j(\omega_k - \omega_r)\underline{\psi}_r^k \tag{2.31}$$

$$\underline{\psi}_s^k = L_s \underline{i}_s^k + L_m \underline{i}_r^k \tag{2.32}$$

$$\underline{\psi}_r^k = L_r \underline{i}_r^k + L_m \underline{i}_s^k \tag{2.33}$$

$$J\frac{\mathrm{d}\Omega_r}{\mathrm{d}t} = \frac{J}{n_p}\frac{\mathrm{d}\omega_r}{\mathrm{d}t} = T_e - T_L \tag{2.34}$$

$$\frac{\mathrm{d}\Theta_r}{\mathrm{d}t} = \omega_r \tag{2.35}$$

$$T_e = \frac{3n_p}{2} Im(\underline{\psi}_s^{k^*} \underline{i}_s^k) \tag{2.36}$$

where $\underline{u}_s^k$ represents complex stator voltage, $\underline{u}_r^k$ complex rotor voltage, $\underline{i}_s^k$ complex stator current, $\underline{i}_r^k$ complex rotor current, $\underline{\psi}_s^k$ complex stator flux, $\underline{\psi}_r^k$ complex rotor flux, R_s stator resistance, R_r rotor resistance, ω_k stator current frequency, ω_r rotor electrical speed, L_s stator inductance, L_r rotor inductance, L_m mutual inductance, Ω_r rotor mechanical speed, J mechanical inertia of the machine, n_p number of pole pairs, T_e electromechanical torque, T_L load torque, and Θ_r mechanical angle of the rotor.

For a detailed circuit separating harmonic components, *Hubert*'s thesis should be consulted [25].

2.6.2 Park and Clarke transformations

Figure 2.10 shows the different coordinate systems the motor can be modeled at, see section A.1 for transformation matrices. *Clarke* and *Park* transformations allow the model to have two phase time dependent variables in a stationary coordinate system ($\alpha\beta$) and two phase stationary variables in a rotating coordinate system (dq), respectively.

2.6.3 Dynamic inverse-Γ model for the induction machine

Even though the model derived in section 2.6.1 clearly describe the physical behavior of the machine, it is not optimal for the control or computerization, due to the

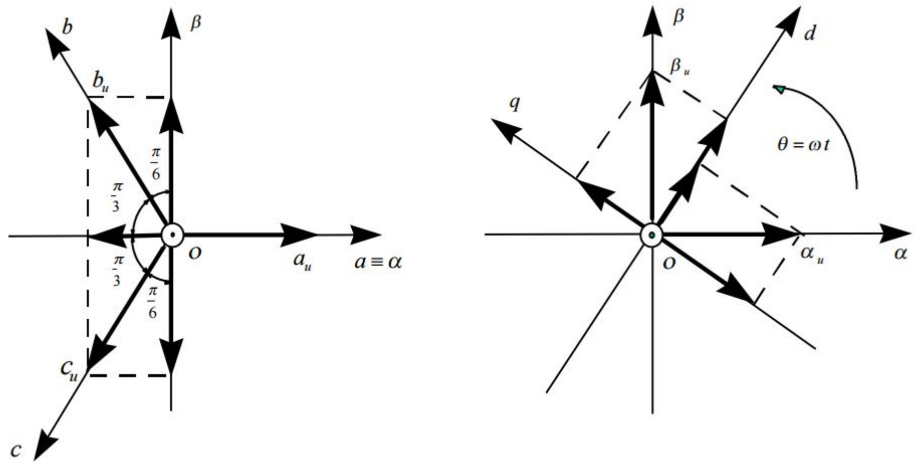

Figure 2.10: Graphical representation of rotating 3-phase system, rotating $\alpha\beta$ system and static dq system

fact that it is over-parametrized. It can be seen that the currents are not linearly independent, as

$$\underline{i}_m^s = \underline{i}_s^s + \underline{i}_r^s \tag{2.37}$$

Then, by creating a new variable, b, as

$$b = \frac{L_m}{L_r} \tag{2.38}$$

and defining new rotor variables

$$\underline{\psi}_R^s = b\underline{\psi}_r^s \tag{2.39}$$

$$\underline{i}_R^s = \frac{\underline{i}_r^s}{b} \tag{2.40}$$

the over-parametrization is corrected and the model becomes the $inverse - \Gamma$ form of the induction machine [22].

2.6.3.1 Stationary reference system

The following equations describe the behavior of the induction machine $inverse - \Gamma$ model, see figure 2.11, in an amplitude invariant reference system. For the reader's added convenience, the mechanical equations of the machine will also be reproduced, even though they remain unchanged [22, 23, 24]:

$$\underline{\psi}_R^s = \frac{L_m}{L_r}\underline{\psi}_r^s \tag{2.41}$$

$$L_M = \frac{L_m^2}{L_r} \tag{2.42}$$

$$L_\sigma = L_s - L_M \tag{2.43}$$

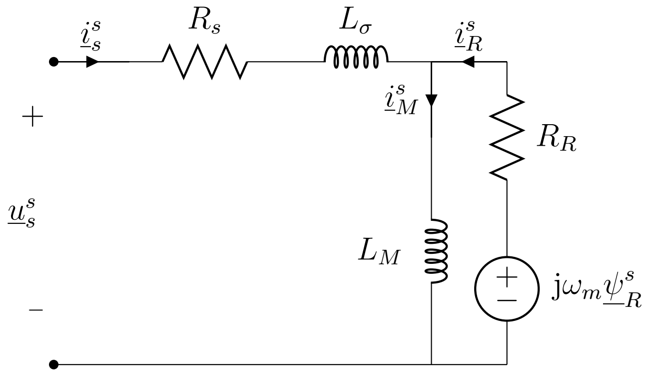

Figure 2.11: Induction machine $inverse - \Gamma$ model circuit diagram in $\alpha\beta$ frame

$$R_R = \left(\frac{L_m}{L_r}\right)^2 R_r \tag{2.44}$$

$$\underline{u}_s^s = L_\sigma \frac{\mathrm{d}\underline{i}_s^s}{\mathrm{d}t} + (R_s + R_R)\underline{i}_s^s - \left(\frac{R_R}{L_M} - j\omega_r\right)\underline{\psi}_R^s \tag{2.45}$$

$$\frac{\mathrm{d}\underline{\psi}_R^s}{\mathrm{d}t} = R_R\underline{i}_s^s - \left(\frac{R_R}{L_M} - j\omega_r\right)\underline{\psi}_R^s \tag{2.46}$$

$$\underline{\psi}_s^s = L_\sigma\underline{i}_s^s + L_M\underline{i}_M^s \tag{2.47}$$

$$\underline{\psi}_R^s = L_M\underline{i}_M^s = L_M(\underline{i}_s^s + \underline{i}_R^s) \tag{2.48}$$

$$J\frac{\mathrm{d}\Omega_r}{\mathrm{d}t} = \frac{J}{n_p}\frac{\mathrm{d}\omega_r}{\mathrm{d}t} = T_e - T_L \tag{2.49}$$

$$\frac{\mathrm{d}\Theta_r}{\mathrm{d}t} = \omega_r \tag{2.50}$$

$$T_e = \frac{3n_p}{2} Im(\underline{\psi}_R^{s*}\underline{i}_s^s) = \frac{3n_p}{2}(\psi_{R\alpha}i_{s\beta} - \psi_{R\beta}i_{s\alpha}) \tag{2.51}$$

where the superscript ^{s} represents $\alpha\beta$ reference frame quantities, $\underline{u}_s^s$ complex stator voltage, $\underline{i}_s^s$ complex stator current, $\underline{\psi}_s^s$ complex stator flux, $\underline{\psi}_R^s$ complex rotor flux, R_s stator resistance, R_R transformed rotor resistance, ω_1 stator current frequency, ω_r rotor electrical speed, L_σ total leakage inductance, L_M transformed magnetizing inductance, L_m mutual inductance, Ω_r rotor mechanical speed, J mechanical inertia of the machine, n_p number of pole pairs, T_e electromechanical torque, T_L load torque, and Θ_r mechanical angle of the rotor.

2.6.3.2 Rotating reference system

After Clarke transformation is performed on the 2.41-2.51 equations, stationary variable equations in rotating reference system are obtained. However, by definition, this reference system aligns the rotor flux, ψ_R, with the d axis, meaning that $\underline{\psi}_R = \psi_R$. Then, the complete set of equations for a perfectly aligned field, with the mechanical and resistance and inductance transformation equations of the machine for the reader's added convenience, even though they remain unchanged, is [22, 23, 24]:

$$L_M = \frac{L_m^2}{L_r} \tag{2.52}$$

$$L_\sigma = L_s - L_M \tag{2.53}$$

$$R_R = \left(\frac{L_m}{L_r}\right)^2 R_r \tag{2.54}$$

$$\underline{u}_s = L_\sigma \frac{\mathrm{d}\underline{i}_s}{\mathrm{d}t} + (R_s + R_R + j\omega_1 L_\sigma)\underline{i}_s - \left(\frac{R_R}{L_M} - j\omega_r\right)\psi_R \tag{2.55}$$

$$\frac{\mathrm{d}\psi_r}{\mathrm{d}t} = R_R \underline{i}_s - \left(\frac{R_R}{L_M} + j(\omega_1 - \omega_r)\right)\psi_R \tag{2.56}$$

$$\underline{\psi}_s = L_\sigma \underline{i}_s + L_M \underline{i}_M \tag{2.57}$$

$$\psi_R = L_M \underline{i}_M = L_M(\underline{i}_s + \underline{i}_R) \tag{2.58}$$

$$J\frac{\mathrm{d}\Omega_r}{\mathrm{d}t} = \frac{J}{n_p}\frac{\mathrm{d}\omega_r}{\mathrm{d}t} = T_e - T_L \tag{2.59}$$

$$\frac{\mathrm{d}\Theta_r}{\mathrm{d}t} = \omega_r \tag{2.60}$$

$$T_e = \frac{3n_p}{2}\psi_R i_{sq} \tag{2.61}$$

where $\underline{u}_s$ represents complex stator voltage, $\underline{i}_s$ complex stator current, $\underline{i}_r$ complex rotor current, $\underline{\psi}_s$ complex stator flux, ψ_r real rotor flux, R_s stator resistance, R_R transformed rotor resistance, ω_1 stator current frequency, ω_r rotor electrical speed, L_σ total leakage inductance, L_M transformed magnetizing inductance, L_m mutual inductance, Ω_r rotor mechanical speed, J mechanical inertia of the machine, n_p number of pole pairs, T_e electromechanical torque, T_L load torque, and Θ_r mechanical angle of the rotor.

2.7 PWM Theory

Inverter fed induction motors, example in figure 2.12, offer various advantages over those fed by the grid directly, such as V/f control, which involves the possibility of working in constant torque, constant power and high speed regions. The disadvantage is the appearance of harmonics in the stator windings, shown in figure 2.13, due to switchings of the inverter. However, the rectifier harmonics will not be considered, as the vehicle is not supposed to move while charging. If the modulation index, m_f, which relates commutation f_c and fundamental f_s frequencies, as

$$f_c = m_f \cdot f_s \tag{2.62}$$

is big enough, $m_f > 30$, the PWM harmonics can be easily filtered. The options to reach higher speeds with a fixed commutation frequency are two: to increase maximum switching frequency of the inverter or to decrease m_f. The first increases losses and cost of the inverter, whereas the second reduces the frequency of the harmonics, making them harder to filter [26].

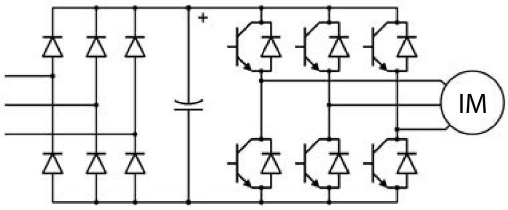

Figure 2.12: System overview with diode rectifier, battery, 3-phase inverter and motor leads

An example of the harmonic distribution of the output voltage waveforms is shown in 2.13. The most significant harmonics are given as

$$m_{f,Vmax} = m_f \pm 2 \tag{2.63}$$

In case these coincide with system resonances, they could be amplified and become a major NVH issue. However, it is very important to note that PWM does not include any new space harmonics into Maxwell forces, but rather varies the magnitude of the existing Maxwell harmonic frequencies [20].

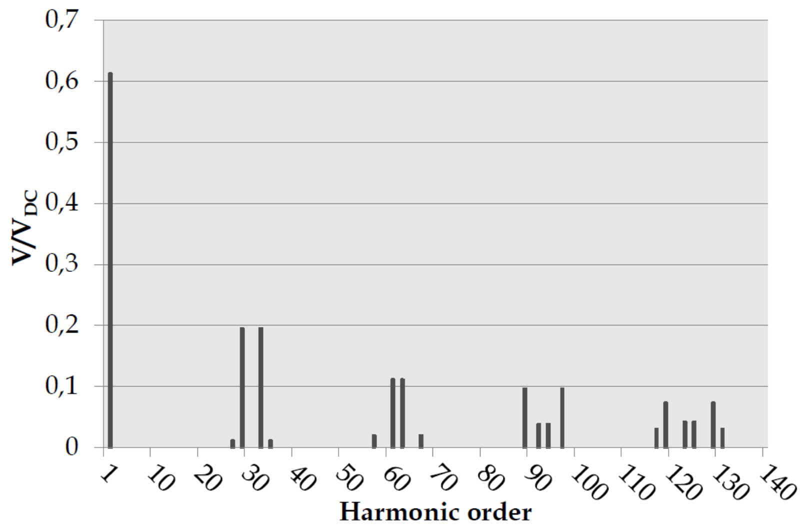

Figure 2.13: 3 phase PWM harmonic distribution, example with $m_f = 31$

As for the distribution of PWM harmonics, *Mohan et al.* [26] state that the main PWM harmonics have spatial orders of $m_f \pm 2$ and $2m_f \pm 1$, if m_f is a sufficiently high number. However, as the inverter application is required to work in a wide range of frequencies, with various m_f, this will be compared with the simulations, as the magnitudes shown in figure 2.13 may vary greatly when m_f has a low value.

2.8 Induction motor losses

The electric motor performance and operation ranges are limited by two factors: heat transfer and mechanical capability of the components. Bearings and system inertia limit the high speed operation of the machine, as mechanical failure of the system cannot be risked, and safety must be guaranteed in this aspect. On the other hand, the heat behavior of the system is affected by many more variables, it is a much more complex issue.

In this context, cooling is critical, as thermal saturation of the materials can occur if the temperature is excessively high. Losses in the machine must be treated as distributed heat sources for optimization of the performance, but a volume averaged heat generation can be enough for an initial approach.

The losses in an induction motor can be expressed as

$$P_{Cu} = \frac{3}{2} R_s I_{s,RMS}^2 \tag{2.64}$$

$$P_{Fe} = k_h f_s B_{max}^n + k_e f_s^2 B_{max}^2 \tag{2.65}$$

$$P_{Fe,PWM} = \sum_i k_h f_i B_{max}^n + k_e f_i^2 B_{max}^2 \tag{2.66}$$

where P_{Cu} represents copper losses, $I_{s,RMS}$ is the input root mean square value current into the stator, P_{Fe} is the iron loss, k_h is a constant related to hysteresis loss, f_s is the supply frequency, B_{max} is the peak value of the magnetic flux density, n is a parameter which depends on the magnetic loading, frequency and material (usually 1.6-2.2) and k_e is a constant related to eddy currents loss.

PWM increases iron losses greatly, as it introduces high-order harmonics, which enhance linearly and quadratically the total iron losses. These can be reduced by using an appropriate PWM switching strategies, as *Miyama et al.* propose [27]

3

Mechanical model of a vehicle: NVH theory

3.1 Introduction

One of the main *NVH* sources in fully electric drives is the motor, due to the fact that the electromagnetic forces excite the motor and driveline housing [6, 28]. The secondary source of the excitation on driveline is mechanical, caused by the machine torque ripple and driveline dynamics [29, 30]. Therefore, torque and forces must be treated as separate excitations, as torque ripple affects the shafts and gearbox, whereas Maxwell forces influence the housing only. The *NVH* characteristics of the motor are mainly described by harmonic excitations leading to high tonalities. This depends on various factors, *e.g.* number of poles and slots, rotor eccentricity and faults in the winding insulation or squirrel cage bars. In some cases, the tonal sounds are also affected by the electrical system and the control unit [6, 31]. However, as the vehicle is not supposed to move while connected to the grid, in opposition to train or tram applications, there will not be influence of the rectifier harmonics in the motor output when the vehicle is moving.

Any noise issue in a structure is always defined by these elements: source, transfer path to the structure and radiating surface. For an accurate evaluation, the three of them have to be carefully modeled and simulated. At early development stage, a hammer test, also called forced frequency response calculation, can be carried out. This method can help evaluate different designs, but does not predict realistic *NVH* problems, as the source is not a realistic scenario. What is more, torque and forces are sources at the same time, and effects on each other should not be neglected. Those two excitations are continously fluctuating, even in steady state, so a much deeper evaluation must be performed, taking transfer path and radiating surface into account.

Due to non-linearities of the system, a fast computation of the analytical models [9] is not enough. Even though accuracy is crucial when computing Maxwell forces, assumptions for speeding up the calculations are usually made, see section 2.3.1. Maxwell forces are not radial if the material is saturated, even locally. This is a great challenge for *NVH* evaluation of electric drivetrains, as calculation is only achievable by advanced *FEM* simulations when taking the saturation and the detailed shape of the stator, rotor teeth and slots into account [6].

During the last decades, multibody dynamic models have greatly evolved from basic models [32] to the most advanced ones [33, 34, 35], where a nonlinear model of the system is required to accurately represent the dynamics.

The consequences of these analysis are that the mechanical system of housing, shafts and gears will cause misalignment of the shaft. This shifting of the axle makes it eccentric, which affects the performance of the electric machine [36,37]. In addition to that, manufacturing tolerances are also an unavoidable part of the physical system and another source of misalignment. The higher the misalignment, the higher the level of the force applied to the system [36].

3.2 Eccentricity

The rotor of an electric motor has always some eccentricity, either due to manufacturing errors or by the dynamic of the rotor and the forces which applies to the shaft and bearings; or both at the same time [6,29]. The different eccentricity types can be summarized as:

1. Eccentricity of rotation axis
   (a) Axis has a tilt angle
   (b) Axis is shifted with a fixed offset
2. Part eccentricity, e.g. the axis is at the center but rotor part is assembled eccentrically
   (a) Rotor core has a tilt angle
   (b) Rotor core is shifted with a fixed offset

Even if the eccentricity does not change the output torque of the motor significantly, the bearing forces and the forces to the stator will be considerably affected, owing to the fact that the gap is not uniform in all the gap circumference. Although the bearing forces of a a perfectly aligned motor are zero, when the eccentricity is present, the situation changes [29,38]. The unbalance force due to mass eccentricity in an electric machine is expressed as

$$F = (m_u r_u + M_r e) \cdot \omega_r^2 \tag{3.1}$$

where F is the force, m_u is the unbalance mass, r_u is the distance between the axis of rotation and the unbalance mass center, M_r is the rotor mass, e is the mass eccentricity, *i.e.* the distance between the principal inertia axis and the axis of rotation, and ω_r the rotation speed [29].

As seen from the equation, the force is extremely sensitive to the rotation speed. This implies that bigger eccentricities can be a negligible problem at low speed ranges, but become very significant at high speeds [39, 40]. In any case, manufacturing or static eccentricities can be corrected by means of several techniques, such as weight balancing in the rotor or by applying axial stress in the shaft before the installation of the rotor. Dynamic eccentricities caused by magnetostriction and/or mechanical vibrations cannot be corrected, but only predicted, detected and minimized by redesigning the housing or machine.

3.3 Transmission and axle

The motor of an electric vehicle is connected to the drivetrain by means of shafts and gears. A multibody dynamic model has been built by *AVL* to investigate the dynamic behavior of the electric vehicle drivetrain. The schematic in figure 3.1 shows the housings in blue, shafts in thick green, bearings as blue triangles and gears in striped green. This model is validated with the software *AVL Excite* for a manual gearbox [35, 41]. A physical representation of this model can be found, as an example, in figure 3.2, where the rear axle of a *BMW i3* is shown. The mapped forces on the stator can be seen in figure 3.3.

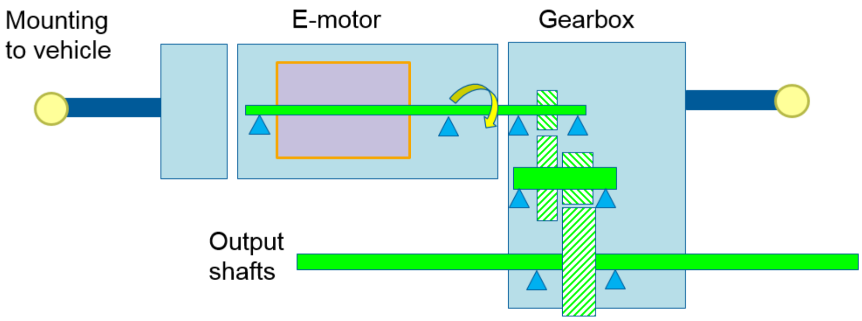

Figure 3.1: Schematic view of the driveline in an electric vehicle. Courtesy of Mehdi Mehrgou.

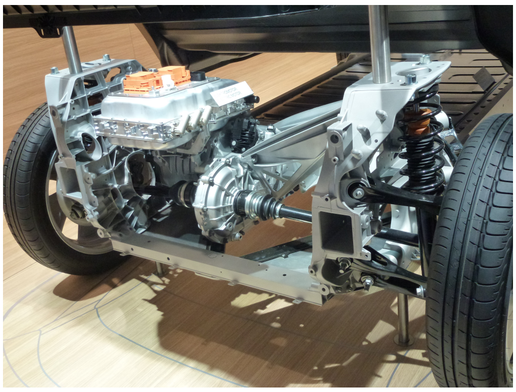

Figure 3.2: Detail of *BMW i3* converter, motor and rear axle © Rudolf Simon

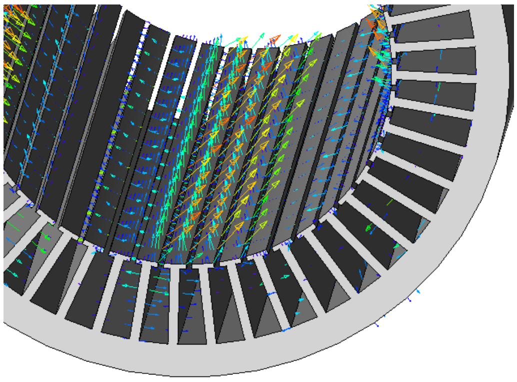

Figure 3.3: Example of mapped electromagnetic forces to the *FEM* frequency domain model. Courtesy of Mehdi Mehrgou.

3.3.1 Shaft and bearings

Ball bearings, displayed in figure 3.4 and most usually in every gearbox and driveline, are great contributors to *NVH* issues. These elements have nonlinear radial, bending and axial behaviors, plus an initial clearance [35, 41]. Axial and radial displacements in the range of some hundred micrometers can be experienced in a shaft mounted with deep grove ball bearings. These vibrations influence the gear contacts and gearbox dynamics, which is another source of shaft eccentricity, see section 3.3.2. Experienced professionals in the company claim that bearing clearances, *i.e.* eccentric shaft or axially displaced inner ring with respect to the outer ring, are critical in the mechanical excitations evaluation applied to the housing. An accurate model developed for multibody dynamic computation of this type of bearing is used in the *AVL Excite* software [35].

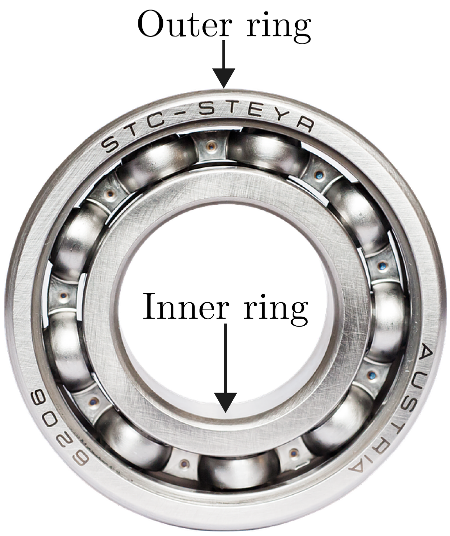

Figure 3.4: Ball bearing inner and outer ring

In any case, the mechanical resonance frequencies of the motor, ω_n, are defined by

$$\omega_n = \sqrt{\frac{\frac{k_1+k_2}{m_1} - \frac{k_2}{m_2} \pm \sqrt{\left(\frac{k_1+k_2}{m_1} - \frac{k_2}{m_2}\right)^2 - 4k_2\frac{k_1+k_2}{m_1 m_2}}}{2}} \tag{3.2}$$

where k_1 is the bearing stiffness, k_2 is the shaft stiffness, m_1 is half of the stator mass and m_2 is the mass of the rotor plus half of the stator mass [29].

The shafts are modeled as flexible components by the coupling of torsional, bending, and axial modes. The dynamics and deflection of shafts are also included in interaction with ball bearings and housing. The amplification factor of the excitation is described as [20]

$$\eta = \frac{1}{\sqrt{\left(1 - \left(\frac{f_r}{f_n}\right)^2\right)^2 + \left(\frac{2\zeta_r f_r}{f_n}\right)^2}} \tag{3.3}$$

where f_r is the frequency at which the amplification is calculated, f_n is $2\pi\omega_n$ and ζ_r is the amplification damping coefficient, defined as

$$\zeta_r = \frac{1}{2Q} = \frac{\omega_2 - \omega_1}{2\omega_n} \tag{3.4}$$

where Q is the quality coefficient of the amplification system, ω_1 and ω_2 are frequencies on either side of ω_n which enclose a band of $3dB$ reduction in the response.

3.3.2 Gearbox

The model uses advanced gear contact systems, accounting for the misalignment and torque fluctuation. As stated in section 3.3.1, these effects create further eccentricity, which should be computed as well for accurate results. The *AVL Excite* software allows the introduction of damping, contact and teeth stiffness and the detailed backlash, micro-geometry included.

3.4 Noise generation

Noise can be defined as unwanted sound. Sound, on the other hand, can be either a vibration wave which propagates though a medium or the perception of the human brain to that wave. Propagation of a sound wave implies time and sound pressure. Then, frequency and pressure are key features when defining a propagating sound wave.

3.4.1 Sound theory

A sound wave can be divided into n waves, each one with a specific frequency, by means of a fast Fourier transform (FFT, see appendix A.2). The total wave pressure, p_{tot}, will be the sum of all waves pressures in the studied frequency spectrum, p_i, as

$$p_{tot}^2 = \sum_{i=1}^{n} p_i^2 \tag{3.5}$$

The sound level, L_p, in dB of a sound wave component is given by

$$L_p = 20 \cdot log_{10}\left(\frac{p_{rms}}{p_{ref}}\right) \tag{3.6}$$

where p_{rms} is the root mean square value of a sound wave pressure and p_{ref} is the reference sound pressure reference, $2 \cdot 10^{-5} Pa$. The total wave sound pressure level results in

$$L_{p,tot} = 10 \cdot log_{10} \sum_{i=1}^{n} 10^{L_{p,i}/10} \tag{3.7}$$

Table 3.1 shows a variety of sound sources and their values in dB, as well as the thresholds of the scale [20]. Levels vary greatly, and can cause temporal or permanent damage in the hearing capacity of individuals and worsen life quality of the nearby houses and office buildings around a road with permanent heavy traffic, for instance.

Table 3.1: Sound pressure levels of various sources

Source	L_p $[dB]$
Theoretical limit at 1 atm pressure	194
Jet engine at 1 meter distance	150
Threshold of pain	130-140
Heavy city traffic	90
Hearing damage (continous exposition)	85
Normal city traffic	70
Normal conversation	40-60
Threshold of hearing	0

However, this approach is not sufficient, as it does not take the human frequency response into account, *i.e.* our hearing ability for each frequency. Weighing curves are used for accounting for that. There are four major weighing curves, named A, B, C and D. A, B and C come from the 40, 70 and 90 phone Isophone curves [42], whereas case D is a special case for airplane use. The selected curve for this application is case A, shown in figure 3.5. This amplification has to be added to the tonal response of the system by simply substituting $L_{p,i}$ for $L_{p,i} + \Delta A_i$ in equation 3.7, where ΔA_i is the weighing curve value in dB at frecuency f_i.

It is noticeable that the amplification has a maximum at around $2.5kHz$, in all weighing curves, which implies that human hearing has maximized capability to detect sounds at that frequency. Furthermore, exposure time plays an important role as well, as $82dB$ during $16h$ is equivalent to $115dB$ during $30s$ [42].

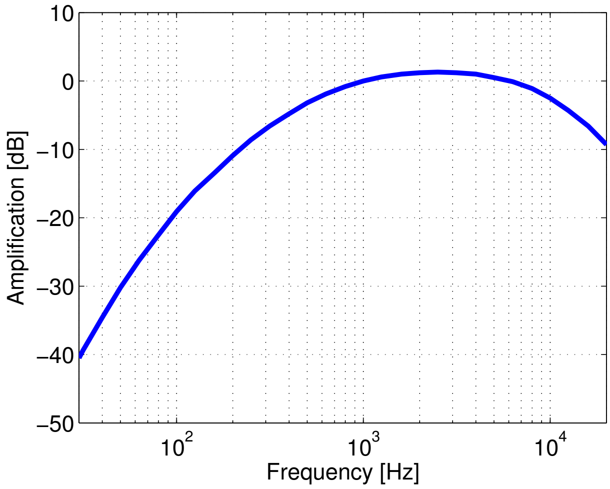

Figure 3.5: A weighing curve amplification in the audible frequency spectrum

To achieve the realistic mode shapes of the structure, the full assembly consisting of the e-motor, stator and housing, in connection with the gearbox, should be modelled. The forces applied on the primary shaft bearings of the housing will also cause deflection at the differential bearings and opposite. These deflections have significant impacts on whine and rattle since they affect the gear contact and backlash. In addition, the whole subsystem should be considered in the model.

3.5 Vehicle dynamics

All previous mechanical theory sections need a framework to be taken into consideration. In automotive applications, vehicle dynamics lay the groundwork for the accounting of all possible scenarios a driver might encounter in real-life driving. Under the assumption that the vehicle has no stability problems and that the vehicle mass is placed at the center of gravity, the forward acceleration will be obtained according to *Newton*'s second law, as

$$\sum F = ma = F_{tractive} - F_{resistive} \tag{3.8}$$

where F is any force in the longitudinal direction, m is the vehicle mass, a is the longitudinal acceleration suffered by the vehicle, $F_{tractive}$ is the total force in the forward direction and $F_{resistive}$ is the total force in the rear direction. Therefore, the acceleration is positive when tractive forces are greater than resistive force, whereas the vehicle will experience a speed reduction when resistive forces are greater than tractive efforts.

3.5.1 Wheel force

The force from the powertrain is transmitted to the tires, so that the vehicle can accelerate with respect to the ground. The total force the wheels transmit, F_{wheel}, can be defined as

$$F_{wheel} = F_{acc} + F_{air} + F_r + F_g \tag{3.9}$$

where $F_{acc} = ma$ is the tractive force required to accelerate the vehicle at the desired rate, F_{air} is the aerodynamic drag resistive force, F_r is the rolling resistance resistive force and F_g is the grading force, which can be either tractive or resistive.

It is assumed that the wheel transmits all its power to the ground, *i.e.* that no slip between ground and wheel exists. These approaches are assumed as reasonable within the time frame of this thesis.

3.5.2 Rolling resistance

Rolling resistance is caused by friction between the tires and the road, and its physical base is the depletion of the rubber, which cases hysteresis in the material [43]. However, this can be a too generic approach, since rolling resistance depends on a wide variety of parameters, such as material, geometry, temperature, pressure, speed, road structure and weather conditions [44]. The rolling resistance force can be analytically studied if simplified to

$$F_r = C_r mg \cos(\alpha) \tag{3.10}$$

where C_r is the rolling coefficient, g is the gravity acceleration constant and α is the road inclination angle in radians. Despite that, $\cos(\alpha)$ is often approximated to unity, as even a high slope does not change the rolling resistance substantially; a slope as big as 20% leads to a $\cos(\alpha) = 0.98$, less than 2% error.

Although equation 3.10 might appear as simple, C_r is not a linear parameter, and can only be estimated through extensive experimental studies. At high speeds, C_r increases quadratically with the speed, but at low speeds only linearly [44].For this study, a constant value is applied, 0.012. High efficiency tires have lower coefficients, 0.007-0.009, whereas in case of racing cars this value can reach 0.2-0.3.

3.5.3 Aerodynamic drag

The impact of wind in the car body causes a force that in the direction of the effective wind, $\overrightarrow{v}_{eff}$ defined as

$$\overrightarrow{v}_{eff} = \overrightarrow{v}_{wind} - \overrightarrow{v}_{car} \tag{3.11}$$

where $\overrightarrow{v}_{eff}$ is the effective wind speed against the car, $\overrightarrow{v}_{wind}$ is the wind speed in the rear direction of vehicle movement, $\overrightarrow{v}_{car}$ is the car speed in the forward direction. For example, if the car goes at $90km/h$ against a headwind of $10km/h$, the effective wind speed is $100km/h$ in the rear direction, whereas if the car experiences the same $90km/h$ with a tailwind of $10km/h$, the effective wind speed is $80km/h$ in the rear direction. Taking this into account, a simple empirical model can be built [45], describing the aerodynamic drag, F_a as

$$F_a = \frac{1}{2}\rho_a C_d A_{eff} {v_{eff}}^2 \tag{3.12}$$

where ρ_a is the air density, C_d is the aerodynamic drag coefficient, A_{eff} is the effective cross sectional area and v_{eff} is the efficient wind speed described by equation 3.11.

The aerodynamic drag can be divided into two components, internal and external drag. The internal drag is caused by air entering cooling inlets, passenger compartment ventilation conducts, etc. The external drag, on the other hand, happens due to viscous friction between the car surface and the air plus the pressure drag caused by the existence of a higher pressure in the front of the vehicle with respect to the rear part. According to *Hucho* [45], the dominant component in a street car is the pressure drag.

3.5.4 Grading force

To represent real-driving conditions, a flat terrain simulation is not a good enough approach. Roads have slopes, and these should be included in the simulation, as a motor does not need the same traction power to accelerate from 0 to $100km/h$ in case of 10% upwards and 15% downwards inclination. The gravitational force which affects the dynamics of the car is mostly the parallel to the road, as

$$F_g = mg\sin(\alpha) \tag{3.13}$$

3.5.5 Driving cycles

As it is impossible to predict human behavior while driving, some controlled scenarios need to be standardized in order to evaluate energy consumption and pollutant emissions. Big efforts have been put to this task throughout the last 50 years, starting in *Los Angeles* in the 1950s and *Paris* in the 1960s. Currently, there are several models for this purpose.

The current European cycle is the New European Driving Cycle (*NEDC*), formed by four repeated *ECE-15* urban cycles plus a *EUDC* extra-urban cycle.

The current Japanese procedures involve the *JC08* cycle, representing a high congestion traffic at less than $80km/h$.

In the *U.S.A.*, the emission calculation procedures include the urban *FTP-75*, highway *HWFET*, aggressive *US06* and air conditioning including *SC03*.

4

Simulation models

4.1 Workflow

In order to see how the harmonics of an induction machine which affect the drivetrain in a hybrid or electric vehicle, several tasks need to be defined.

1. FEM simulation of the machine
2. Harmonic analysis of forces and torques for *NVH* evaluation
3. Force mapping and torque export to Multi-Body Dynamics model
4. Feedback of rotor eccentricity
5. FEM simulation of the machine including shaft displacement

Figure 4.1 is a graphical representation of the *NVH* analysis workflow in the *AVL* Power Train Engineering Multi-Body and *NVH* Simulation department. This thesis focuses on the motor design and *FEM* modeling, with a slight insight into the *1D* model for driving cycle simulations.

4.2 FEM simulation of the machine

This section deals with the software setup for the motor design and *FEM* evaluation. In addition to that, appendix A.3 contains the motor design table, figure A.2, and the slot wiring diagram, figure A.1.

4.2.1 Materials

As seen in table 4.1, the chosen core material for the machine design is *JFE Steel 50JN1300* laminated steel, with the BH-curve from figure 4.2a and the iron loss characteristics from figure 4.2b. This material was chosen by the project leader in *AVL*. The coils are made of copper and the squirrel cage of aluminium.

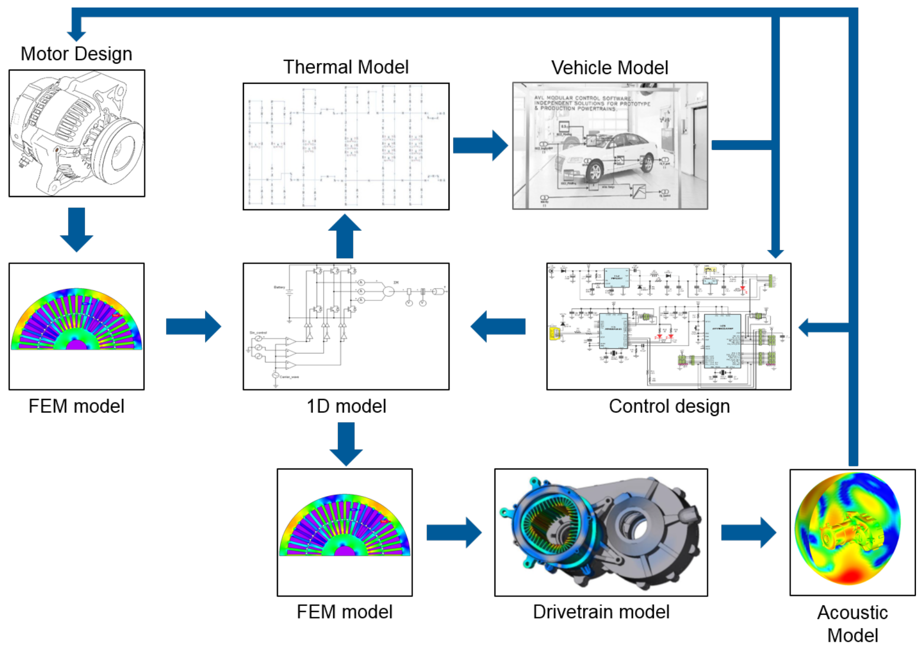

Figure 4.1: Graphical representation of the workflow for *NVH* evaluation of an electric motor

Table 4.1: Material table

Part	Material
Coils	Copper
Cage	Aluminium
Stator core	*50JN1300*
Rotor core	*50JN1300*
Shaft	Air

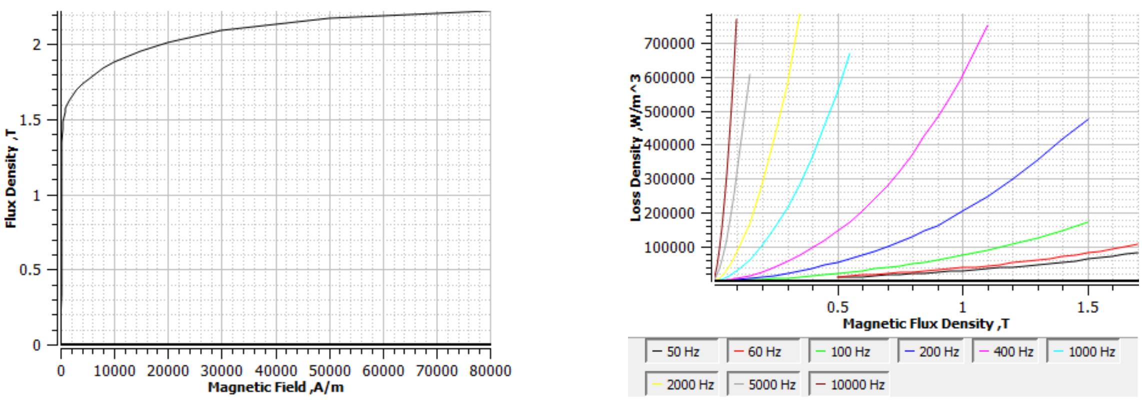

(a) Core material *BH*-curve **(b)** Core material loss curves

Figure 4.2: *JFE Steel 50JN1300* material characteristics from *JMAG*

4.2.2 Electric equivalent circuits in JMAG

The electric equivalent circuit used by *JMAG Express* in order to evaluate the design as a first step is displayed in figure 4.3, and the symbols are explained in table 4.2. However, the use of this tool is not sufficient, as it does not account for local saturation, harmonics or low-slip operation. This tool has a very user-friendly interface aimed at the first stage of machine design, with steady state evaluations every 5% slip.

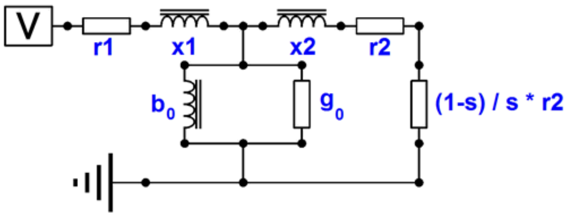

Figure 4.3: *JMAG Express* T-type steady state equivalent circuit

Table 4.2: T-type steady state equivalent circuit parameters from figure 4.3

Variable	Description	Unit
r1	Primary resistance	[Ω]
x1	Primary leakage reactance	[Ω]
r2	Secondary resistance	[Ω]
x2	Secondary leakage reactance	[Ω]
$\mathbf{g_0}$	Iron loss equivalent conductance	[S]
$\mathbf{b_0}$	Excitation susceptance	[S]
(1-s)/s * r2	Rotation equivalent resistance	[Ω]

Once a preliminary design is finished, a *FEM* validation is performed in *JMAG Designer*. The model can be easily transferred from one tool to another and vice versa. The equivalent circuit used for the machine evaluation can be seen in figure 4.4a, detailed stator windings in figure 4.4b and detailed cage bars (*FEM conductor*) and end-rings ($R1$ and $R2$) in figure 4.5.

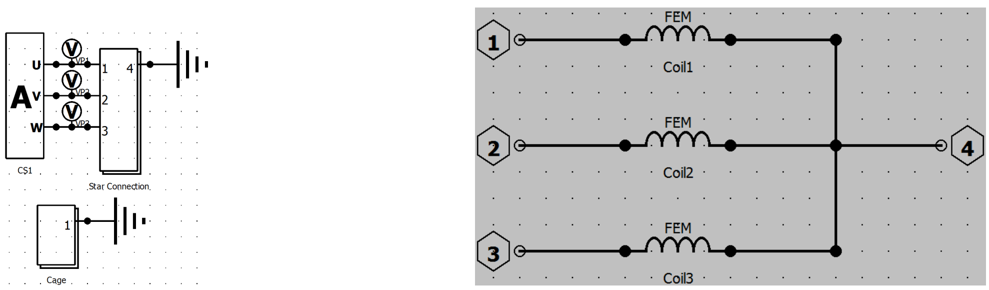

(a) Full circuit

(b) Detail of the star connection block

Figure 4.4: *JMAG* electric interface circuits

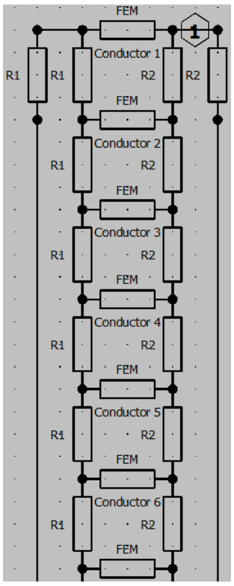

Figure 4.5: *JMAG* electric interface circuit: detail of the cage

4.2.3 Study properties

The studies are set as time transient analysis, with the built-in *Steady-State Approximate Transient Analysis* slip settings and the *Output 1st Step as Steady Result* box checked to help the convergence be faster. The maximum number of iterations is chosen to be 5000, and maximum 30 of them non-linear with the *Newton-Raphson* Relaxation Factor 2 method.

4.2.4 Parametrization of study variables

The variables to be set as study parameters are then input as values or equations. The supply frequency,f here, is input as a number, as the slip, s, maximum current the motor absorbs, I_{rated}, and step time, t_{step}. The rest of variables are set as equations, dependent on these 4 input numbers. Then, the applied current for a study, I_{sweep}, is

$$I_{sweep} = I_{rated} \frac{s}{s_{rated}} \tag{4.1}$$

The end time, t_{end}, is defined as 5 synchronous mechanical rotations, which in mathematical terms can be expressed as

$$t_{end} = 5\frac{2}{f} \tag{4.2}$$

The number of steps for the study, *steps*, is

$$steps = \frac{t_{end}}{t_{step}} \tag{4.3}$$

The rotation speed, n, is set as

$$n = \frac{60}{p} f(1 - s) \tag{4.4}$$

4.2.5 Study conditions

As for the study conditions, *FEM Coil* conditions are applied for each phase, grouping all conductors per phase and pole and giving them the upward or downward direction. This will compute for the copper losses.

A *Rotation Periodic Boundary* is used due to the symmetry in the machine, in order to reduce the model size to half. A *Motion Rotation* condition is applied to the shaft, rotor core, cage and sliding air-gap regions. A *Slide* condition is applied to the air-gap which is included in the *Motion Rotation* condition. To obtain torque and force results, *Torque: Nodal Force* and *Force: Nodal Force* conditions are set to the shaft and stator core, respectively. Besides, a *Symmetry Boundary* is applied to the external air boundary, to limit the analysis region.

The *Iron Loss Calculation* condition is used to compute the core losses, both Joule and Hysteresis components. There, the rotation speed is input, with application of the hysteresis loop and the maximum value of Joule loss.

Last but not least, a *Group (FEM Conductor)* condition is applied to the squirrel-cage bars, which will be used to obtain Joule losses in the cage bars. If the *Group (FEM Conductor)* and *FEM Coil* conditions are correctly set, a link between the circuit in figure 4.4a and the model conditions will be made, and, therefore, electric circuit and *FEM* simulation interfaces will work in parallel.

4.2.6 Meshing of the Induction Machine

In order to evaluate an *FEM* model, meshing is a crucial issue. As the default mesh in *JMAG* is too coarse and does not provide the user with the expected accuracy, it needs to be refined. However, this topic has no unique solution, and the mesh is usually judged as reasonable or excessively coarse or fine by experienced simulation engineers themselves. Figure 4.6 shows the suggested mesh setup by the software supplier's support team in Europe, currently a company named *Powersys*. The full mesh with air regions can be seen in figure 4.6a, whereas a detailed view of the airgap region is also displayed in figure 4.6b. This mesh has various element sizes, $2mm$ for rotor bars, $2.5mm$ for stator windings and $3.5mm$ for stator and rotor cores. The edge mesh around the air gap has an element size of $0.3mm$, and the air gap is divided into 5 radial divisions and 550 circumferential divisions, giving a ratio of 3.06 elements/degree or one element per 19 minutes and 38.2 seconds.

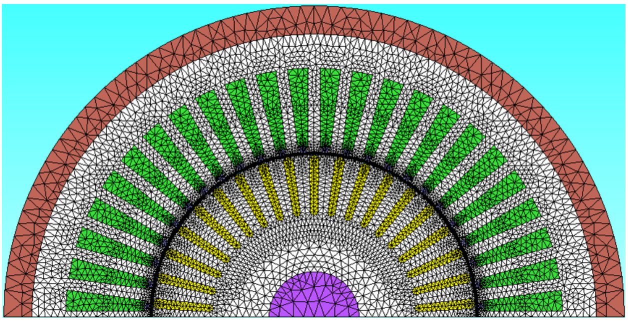

(a) Full mesh

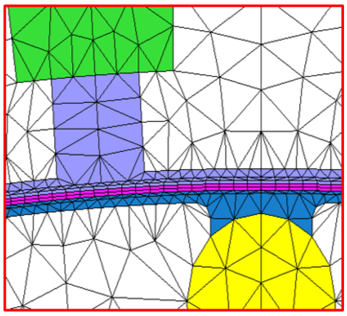

(b) Detail of the mesh

Figure 4.6: Mesh setup with suggestions from *JMAG* Support Europe - *Powersys*

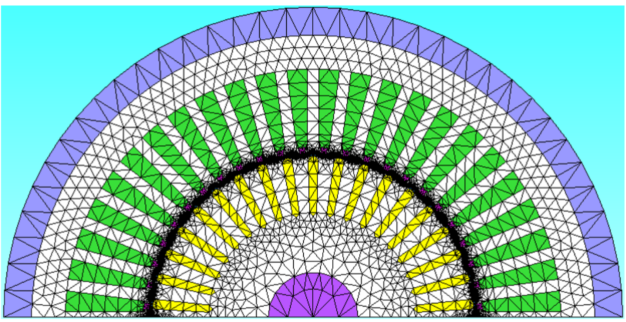

(a) Full mesh

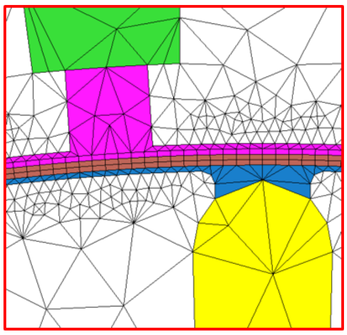

(b) Detail of the mesh

Figure 4.7: Reduced mesh setup

After this mesh was used for a wide range of slip, supply frequency and currents, it was seen that the mesh was too dense, and the studies too time consuming. For example, a time transient magnetic analysis with 2 steady state periods of the supply frequency supposed $4h12min$. Thus, a reduced mesh is proposed. In the studied motor model, a reduction of the number of elements to 1/3 of the original can mean a 1/2 reduction of the elapsed time for a study. As a consequence of this valuable reduction, a new mesh setup, see figure 4.7, is considered, where the stator core, rotor core, stator windings and cage bars have the same element size, $6mm$. The edge mesh around the air gap is kept fine, with an element size of $0.4mm$. The air gap mesh is the same as in the previous case.

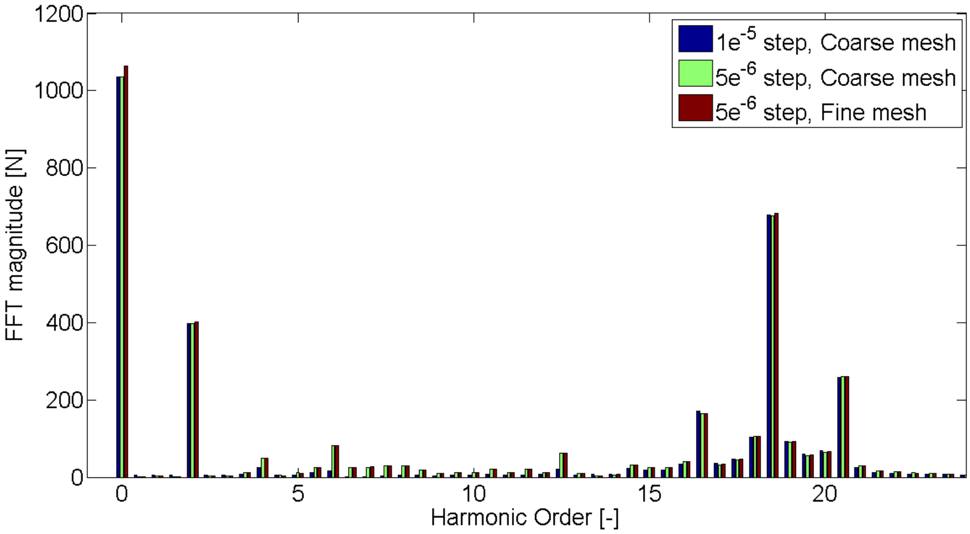

Figure 4.8: Comparison between different step sizes and meshes for a given force *FFT* evaluation

This element reduction greatly enhances the speed of the simulation while keeping the results accurate enough in the 0-50th harmonic order range, see figure 4.8. As this is the audible noise spectrum, there is no need of going higher in frequency for an *NVH* evaluation, and, thus, higher order harmonics are not be considered.

4.3 Multi-Body Dynamics model of the complete drivetrain

For a correct analysis of the drivetrain and the *NVH* issues in it, all components must be included, such as shafts, housings and bearings. Figure 4.9a shows the electric drive shaft, rotor, stator and housing, whereas in figure 4.9b the whole drivetrain housing structure is displayed.

Once all these geometries have been imported in *AVL Excite* software, the resulting Multibody Dynamics model, figure 4.10, can be evaluated.

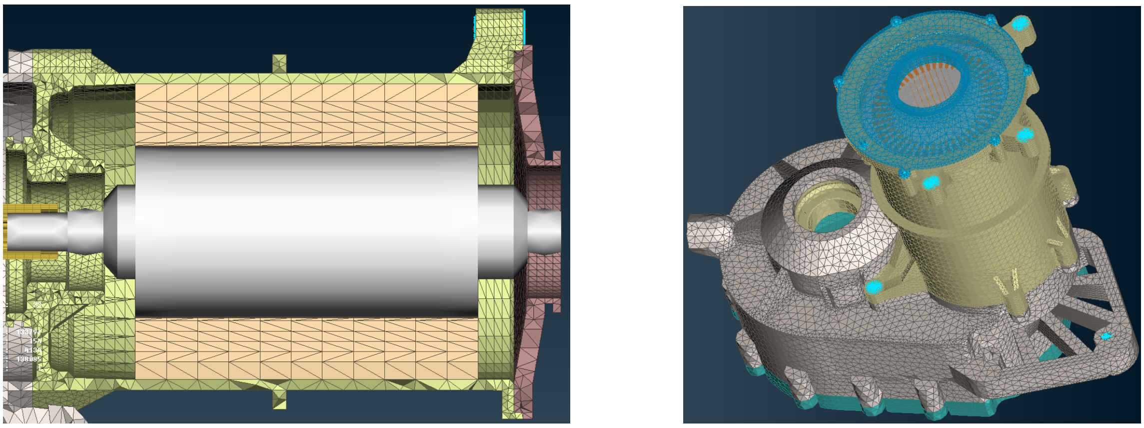

(a) Machine housing and mesh

(b) Drivetrain housing and mesh

Figure 4.9: Complete housing system to be studied. Courtesy of Gergő Gömöri [46].

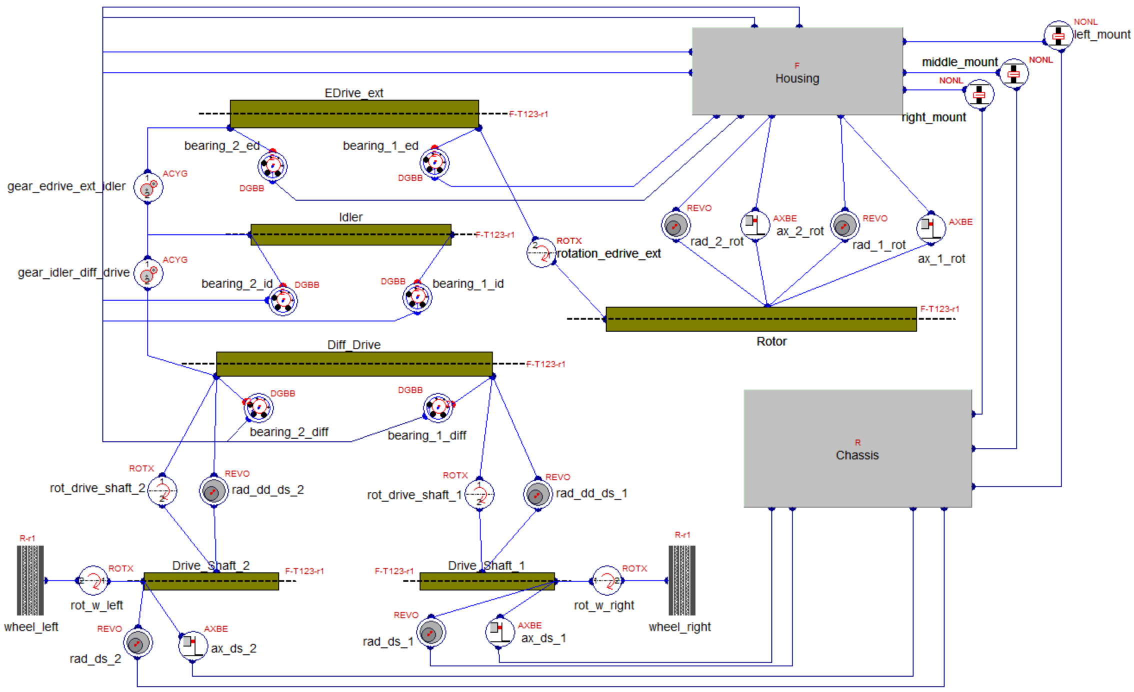

Figure 4.10: Multibody Dynamics *AVL Excite* model. Courtesy of Gergő Gömöri [46].

4.4 Campbell diagram as NVH evaluation tool

The Campbell diagram is one of the main tools in acoustical engineering for identification of a system's response spectrum in the frequency domain. The diagram consists of a pictorical representation of fundamental rotation and its harmonic frequencies. It is named after *Wilfred Campbell* [47], a turbine draftsman and engineer who was responsible of introducing this analysis tool during his work at the *General Electric Company*. This tool is widely used for *NVH* evaluations in rotating machines.

Figure 4.11 shows the potential magnetic flux density Campbell diagram of an induction machine, in case of a 2 pole-paired machine with 48 stator slots and 38 rotor bars. The theoretically potential harmonics for magnetic flux density are $2nd$, $6th$, $18th$, $20th$, $23rd$, $25th$, $37th$, $39th$, $47th$ and $49th$. Therefore, the Maxwell force potential harmonics, displayed on figure 4.12, are in orders $0th$, $2th$, $17th$, $19th$, $21th$, $22th$, $24th$, $26th$, $36th$, $38th$, $40th$, $46th$, $48th$ and $50th$.

This plot does not show the amplitude of each harmonic or the vibration/noise it generates, neither does it take into account factors such as manufacturing tolerances. Therefore, this figure is a simplified guideline of potential harmonics in an electric machine.

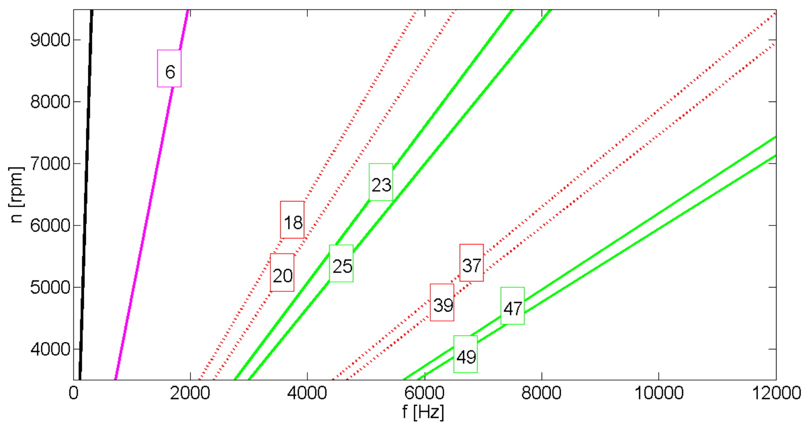

Figure 4.11: Potential magnetic flux density Campbell diagram of the induction motor with $Z_s = 48$, $Z_r = 38$ and $p = 2$. Fundamental in black, saturation in magenta, rotor in red and stator in green.

One of the main reasons to use Campbell diagrams is that mechanical resonances can be easily predicted and detected by means of this representation. For this, the natural or resonance frequencies are represented as vertical lines. Then, crossings of torque and force harmonics with these vertical lines are marked as potentially harmful operation points.

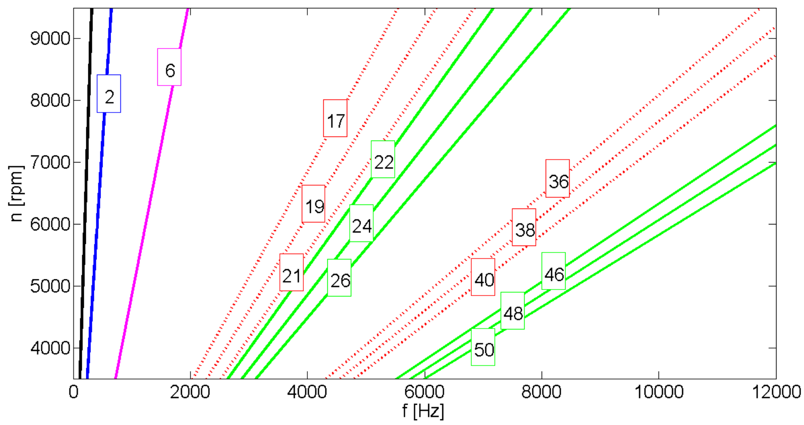

Figure 4.12: Potential force Campbell diagram of the induction motor with $Z_s = 48$, $Z_r = 38$ and $p = 2$. Fundamental in black, force harmonic in blue, saturation in magenta, rotor in red and stator in green.

4.5 Control of the Induction Machine

Control techniques for electric drives have been involved in a great development in the last 20 years with the arrival of faster and more powerful computational capacity. Novel approaches such as the one proposed by *Toyota* [48] have appeared with the wide speed range needs of electric mobility. In this method, the transition between *PWM* and Square Wave has to be as smooth as possible to avoid torque discontinuities. The goal of the control is to make the induction machine work with Maximum Torque Per Ampere (*MTPA*) in the base speed region and Maximum Torque Per Voltage (*MTPV*) in the high speed or field weakening range [49, 50]. Although some approaches have been conducted in this field [51, 52, 53], many have not considered *NVH* as a key issue. Others, have done so with *PMSM* [54] or railway induction motors [6], a much bigger power scale.

However, information from professionals in the company suggested that current (June 2016) vehicle inverters have maximum commutation frequencies of around $10kHz$, meaning that only speeds under $5000rpm$ can be reached while m_f<30 in a 2 pole-paired machine. Thus, either multi-speed gearboxes or lower modulation indexes are unavoidable for operating the machine system under high speed conditions. As the added weight and cost of including a gearbox in the vehicle is unwanted, a lower modulation index will be applied, involving a bigger harmonic content in the supply to the motor when operating in the high speed region. However, it is perceived by experienced professionals in the company that at speeds greater than $80km/h$, the external noise, such as the wind impact on the car or the friction between wheels and road, becomes predominant. Hence, it is assumed that the additional harmonics will not create harmful noise when fed into the motor at high speed conditions.

The control will pursue to follow the guidelines from figure 4.13, with the three regions shown: constant torque, constant power and high speed. In the constant torque region, the current and torque are constant at a given slip and only limited by the thermal limits, whereas voltage and power increase linearly. This allows the voltage to be proportional to the supply frequency, *i.e.* a constant flux or V/f operation.

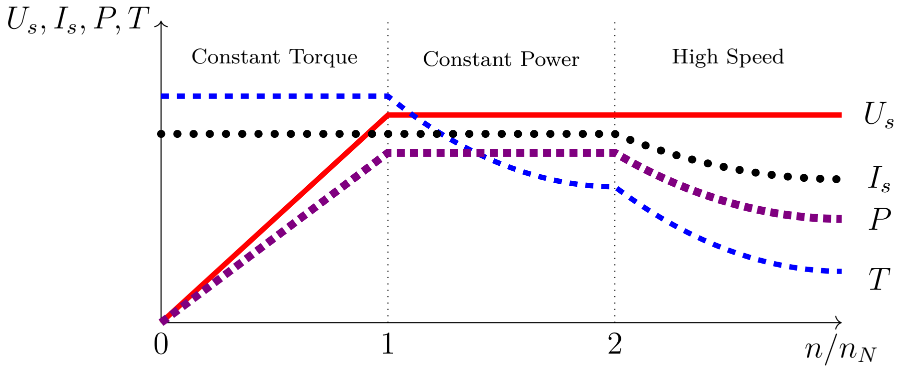

Figure 4.13: Inverter-fed motor ranges of operation

When the supply voltage reaches the machine rated voltage, the constant torque region ends and the constant power region begins. Voltage, current and power are constant, but torque is reduced by a reason of $1/f$. This reduction is due to the flux, proportional to the ratio V/f, being reduced. As voltage has a constant value, rated voltage, and frequency increases, V/f decreases by a factor of $1/f$, and so does the torque, directly proportional to the flux.

When the machine rotates at more than double the rated speed, it enters the high speed region. Here, the current is reduced to decrease the magnetization by means of a lower rotor flux, which allows the motor to reach higher speeds by decreasing the d axis current. The reduction of the current in this axis implies a reduction in the total current, and, therefore, in the rotor flux see section 2.6.3.2 and equation 2.58. As a consequence, the torque will also be reduced, see equation 2.61.

5

Induction Machine design evaluation

5.1 Motor steady state performance

To evaluate this motor, steady state analysis are performed at first. With the aid of the *JMAG Express* tool, a so called *Power Mode* evaluation is carried out. This allows the user to get results for the low slip region, as the default *Quick Mode* calculates values every 5% slip. The outcome of this *Power Mode* evaluation can be seen in figure 5.1 for the torque-speed diagram and figure 5.2 for the efficiency-speed case. Inverter-fed machines work in the low slip range (less than 5%) due to the high efficiency and linear correlation of torque and slip in this region. Whereas figure 5.2a shows the full range of speeds, a detailed view can be seen in figure 5.2b.

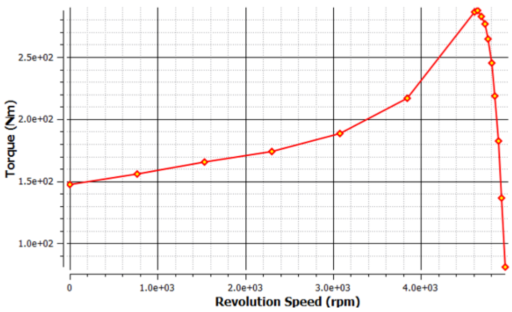

Figure 5.1: Steady state torque-speed characteristic of the motor at 167Hz

Once this is done and the motor design is validated, a broader evaluation is performed. A 0-500Hz sweep is done together with a 1-3% slip sweep. A sample of the results is shown in figure 5.3. However, it can be easily deduced that these plots do not only depend on speed or frequency, but also on slip or current. Thus, a 3D surface plot would be a more thorough approach.

Surface plots are created in this manner. Results from *JMAG* are exported as a matrix, depending on slip and frequency in this case. Then, a linear interpolation is performed with a resolution of 200 points per variable, *i.e.* one point per 2Hz and 0.01% slip. The mechanical variables, torque and mechanical power into the shaft, can be seen in figure 5.4.

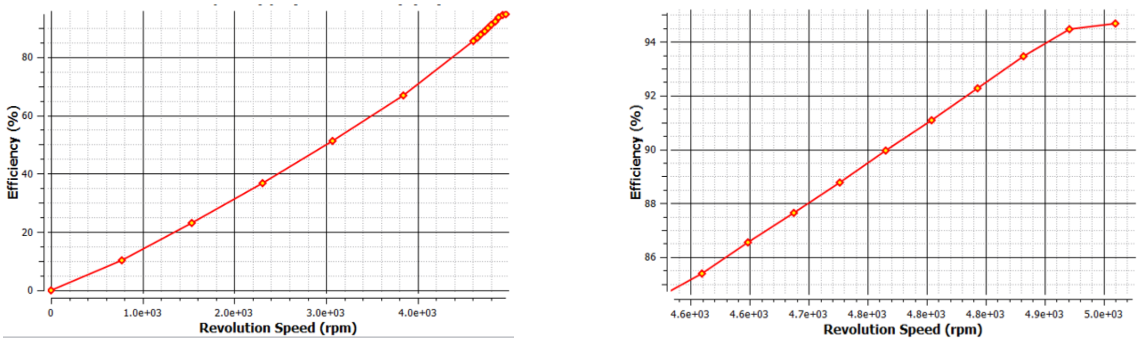

(a) Full speed range

(b) Detail of the 4500-5010rpm range

Figure 5.2: Steady state efficiency-speed characteristic of the motor at 167Hz

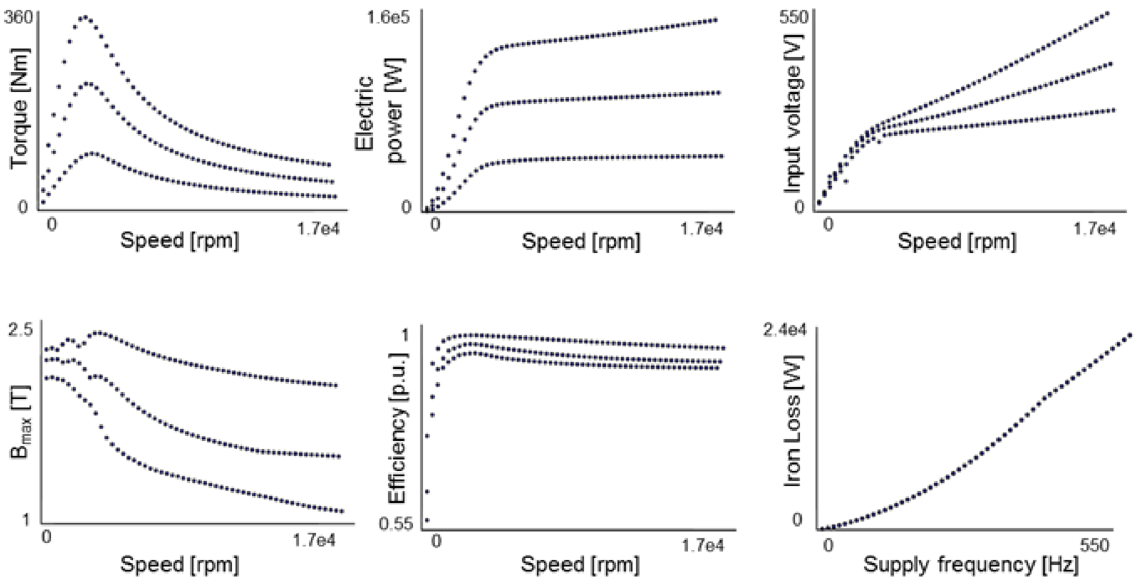

Figure 5.3: Steady state characteristics of the motor with speed and slip sweeps

From the surface plot in figure 5.4a, it can be deduced that torque depends linearly on slip. This is due to the fact that the input current magnitude is set as directly proportional to slip. It can be seen that mechanical power, defined as the product of torque and rotation speed, is linearly dependent on both slip and supply frequency, see figure 5.4b.

The inverter rating variables, *i.e.* voltage, current and apparent power in their *RMS* values are displayed in figures 5.4c, 5.4d and 5.4e, respectively. As mentioned above, current is set to be directly proportional to slip. Voltage grows linearly in the low frequency range for all slips, but continues to further grow in the high-slip high-frequency range. Apparent power, product of current and voltage, grows linearly for all slips in the low frequency range. Furthermore, this variable further grows linearly with slip for medium and high frequencies.

The losses and efficiency are mapped as well in figures 5.5a, 5.5b and 5.5c. Iron losses have a similar behavior to that of voltage, with a linear growth in the low frequency range for all slips, and further growth in the high-slip high-frequency range. Copper losses follow the same behavior pattern as apparent power. As far as efficiency is concerned, it has low values in the low frequency range, mainly due to the lack of voltage boost in this region. Apart from that, it holds values over 88% in the rest of operation points.

Last but not least, the electromagnetic variables of the motor, maximum magnetic flux density and phase coil inductance, are shown in figures 5.5d and 5.5e, respectively. Magnetic flux density tends to decrease as frequency increases, due to the back-*EMF* of the machine increasing with frequency and opposing the growth of the magnetic flux density magnitude. On the other hand, coil inductances decrease as frequency and slip increase.

5.2 Simulation of speed run up

By means of a tool of the *JMAG* software suite, *JMAG RT Viewer*, a steady state torque-speed diagram of the machine when driven by an inverter can be obtained, see figure 5.6.

This torque profile can be applied to a vehicle model in order to evaluate the speed run up it would cause. Several analysis are carried out, such as a comparison between different weights and gear ratios. Figure 5.7 contains an example of these comparisons, where two vehicles with masses of $1400kg$, in blue, and $2200kg$, in red, use a 12.5 gear ratio. It is seen that the lighter mass implies a greater acceleration, and reaches $100km/h$ in 6.6 seconds, whereas the heavier car needs 9.9 seconds.

Another interesting result is displayed on figure 5.8. Here, four different gear ratios are compared in the $1400kg$ vehicle. The original 12.5 ratio is in blue and modifications to 6 in red , to 8 in green and to 10 in black. A very noticeable conclusion

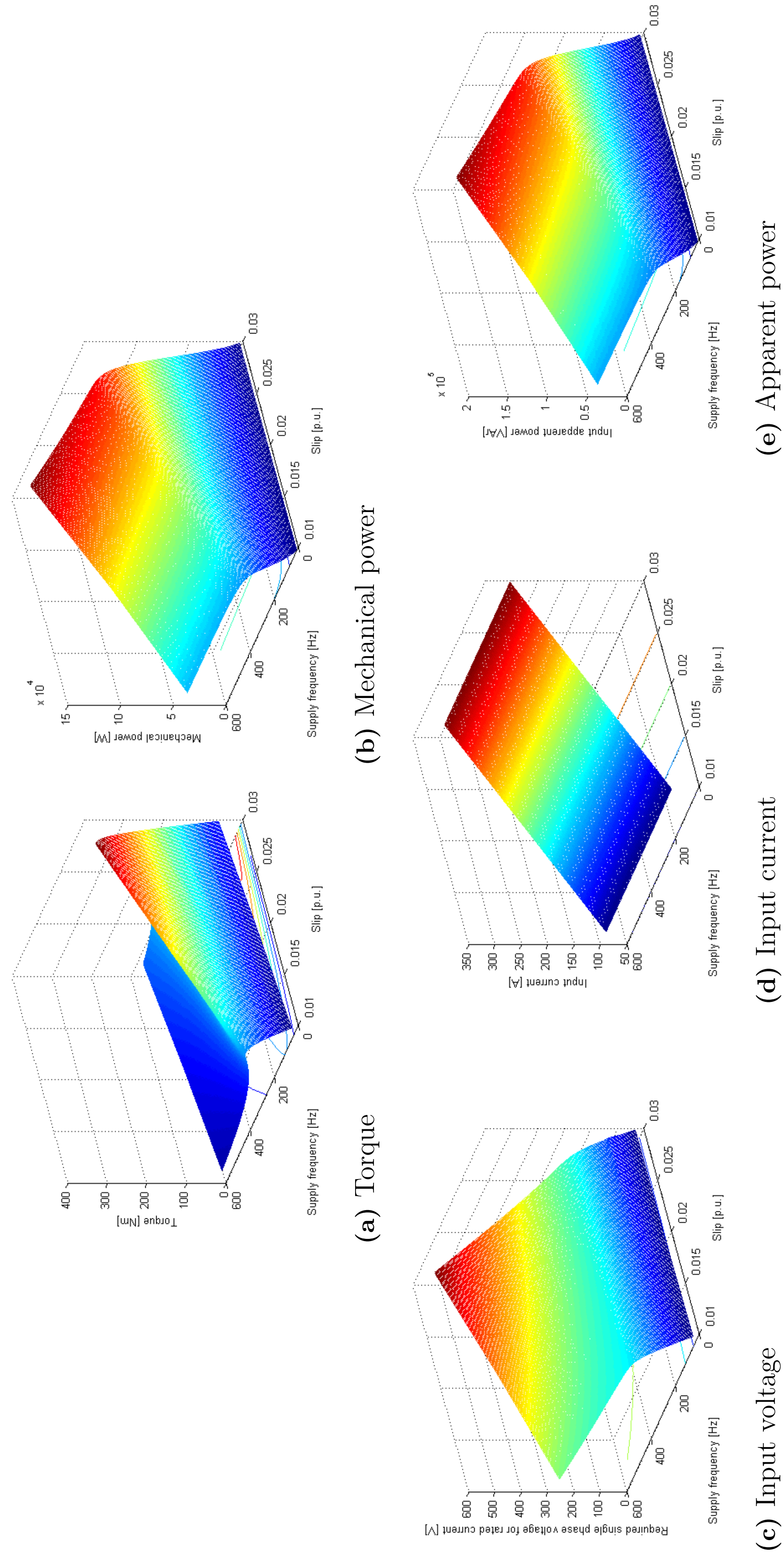

(a) Torque

(b) Mechanical power

(c) Input voltage

(d) Input current

(e) Apparent power

Figure 5.4: Surface plots of steady state motor analysis: mechanical and electrical variables

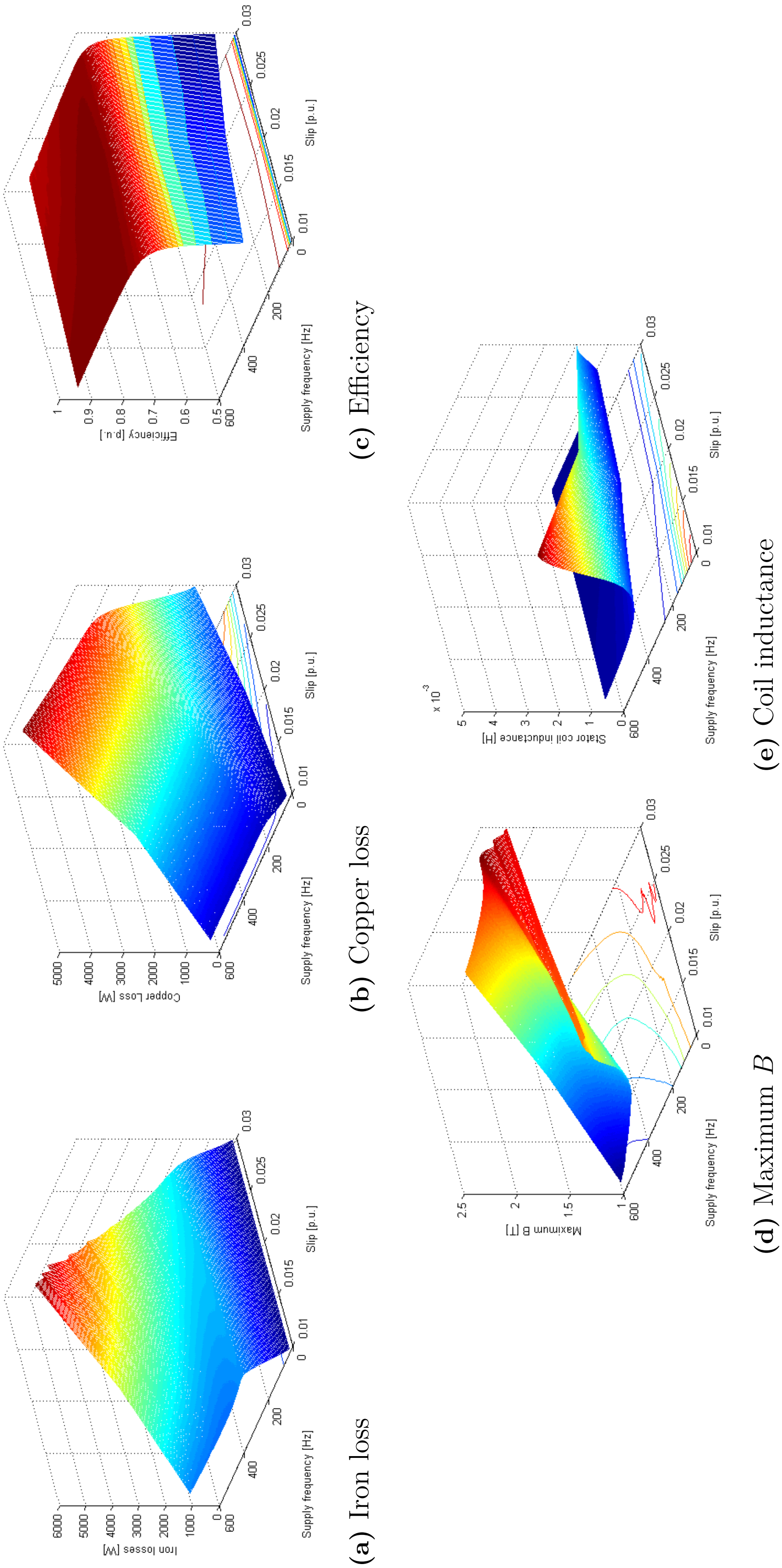

(a) Iron loss

(b) Copper loss

(c) Efficiency

(d) Maximum B

(e) Coil inductance

Figure 5.5: Surface plots of steady state motor analysis: loss and magnetic variables

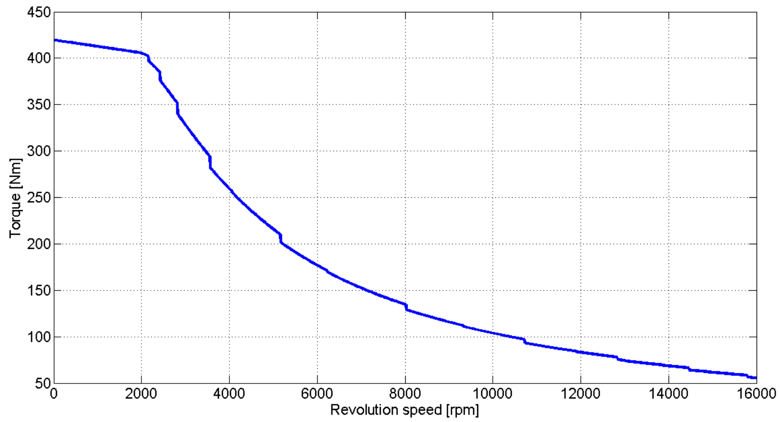

Figure 5.6: Torque diagram for the inverter-driven induction machine

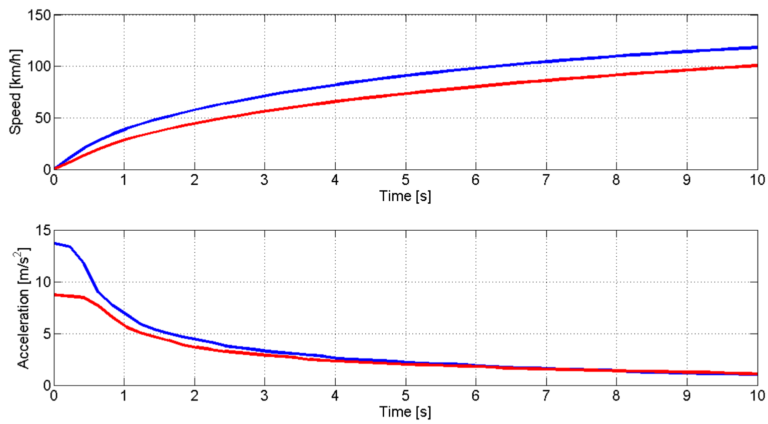

Figure 5.7: Speed run up response of vehicle with 12.5 gear ratio. Masses: $1400kg$ in blue and $2200kg$ in red

is that the black curve has a lower initial magnitude of the acceleration, but it becomes larger than the original from $t = 0.5s$. The green curve overcomes the blue at $t = 0.7s$. The 12.5 ratio is the fastest until $t = 1.3s$, where the ratio equal to 10 becomes the fastest. 12.5 is faster than 8 until $t = 4.8s$, and from then on, the lower gear ratio is faster.

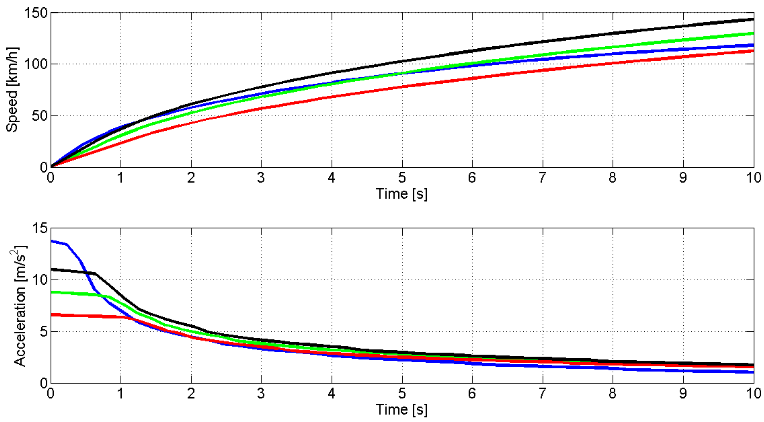

Figure 5.8: Speed run up response of vehicle with $1400kg$ mass. Gear ratios: 6 in red, 8 in green , 10 in black and 12.5 in blue

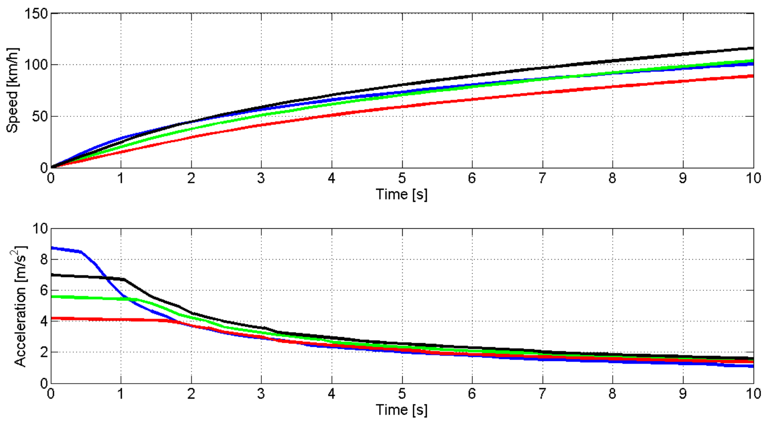

Figure 5.9: Speed run up response of vehicle with $2200kg$ mass. Gear ratios: 6 in red, 8 in green , 10 in black and 12.5 in blue

Figure 5.9 contains an analogous evaluation for the $2200kg$ vehicle. The color code is the same as in the $1400kg$ case. With this heavier vehicle, the differences between different gear relations are larger, due to the bigger mass of the vehicle. The lowest gear ratio has a lower initial magnitude of the acceleration, but it becomes larger than the original from $t = 1.8s$. However, it does not catch up in the speed plot, since the integral of the acceleration difference is very noticeable in this 0-1.8s range. When the original 12.5 is compared with the 8 ratio, both speeds are equal at around $t = 7s$, and from then on, the lower gear ratio is faster. The fastest setup is the one with a relation of 10, as its acceleration becomes the greatest of the four at $t = 0.8s$, and the speed overcomes the original at $t = 2s$.

From the analysis shown in figures 5.8 and 5.9, and three additional analysed ratios, a *0-100km/h time* comparison is carried out. This study is displayed on figure 5.10, and it is seen that the lighter car reaches $100km/h$ faster than the heavier one in every case. The time experiences a non-linear decrease as the gear ratio increases. However, there is a minimum in 11. With bigger radios than the optimum, the time increases with a steeper slope than that of the lower ratios. The fastest responses are $4.3s$ for the $1400kg$ vehicle and $6.9s$ for the $2200kg$ case. These times imply reductions of $2s$ and $3s$, respectively, compared with the original 12.5 ratio.

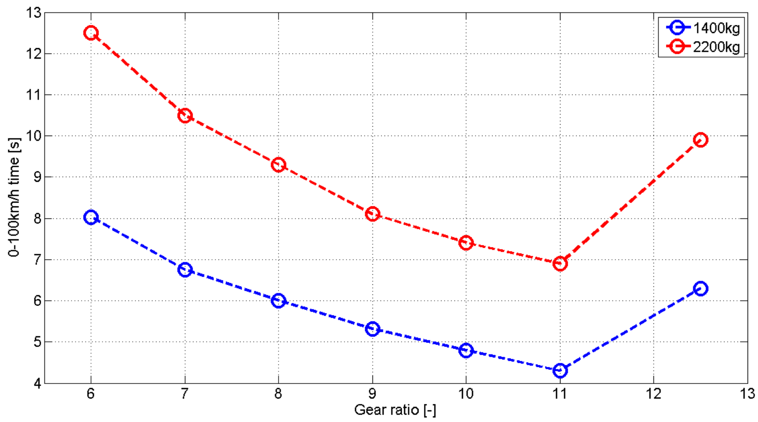

Figure 5.10: 0-$100km/h$ time response of vehicle with $1400kg$ mass, in blue, and with $2200kg$ mass, in red

In order to verify if the mass difference has any non-linear effect, a mass harmonized analysis, see figure 5.11, is also performed. It is noticeable that mass does only influence acceleration in a linear way, since the maximum deviation is 3.1% with the gear relation equal to 9. The major implication of this consequence is that any drivetrain can be optimized for a wide variety of weights. The $1400kg$ vehicle experiences an improvement of 31.76% in the 0-100 time/mass ratio, whereas it is 30.31% in case of the $2200kg$.

5.3 Driving cycle losses

The results of the driving cycle heat loss assessments are presented in figures 5.12, 5.13 and 5.14, with the speed profiles on top, losses in the middle and electric power in the motor in the bottom. A positive power means motor operation, whereas a negative power is an indicator of regenerative braking.

The vehicle configuration used for this analysis is a $2200kg$ mass, 10% of rotating mass, $2.4m^2$ front cross section, $0.547m$ wheel diameter, 0.3 drag coefficient and 0.008 rolling friction coefficient. As far as the transmission is concerned, a gear ratio of 8 is chosen, with an efficiency of 98% and $50W$ friction losses.

The electric drive average efficiency during different driving cycles is found logical, as

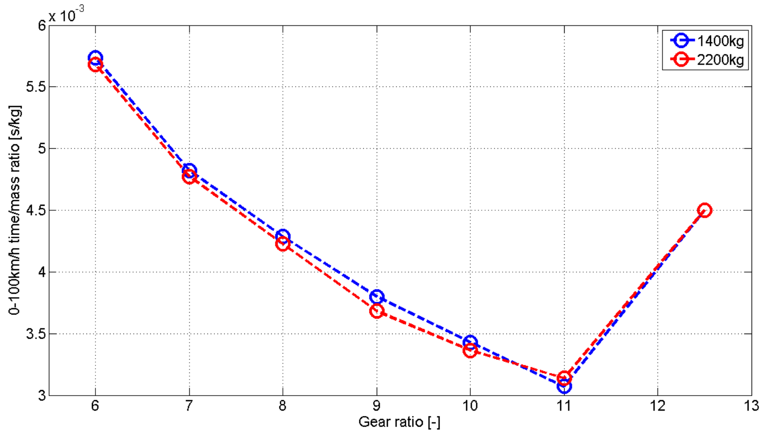

Figure 5.11: Mass harmonized 0-100km/h time response of vehicle with 1400kg mass, in blue, and with 2200kg mass, in red

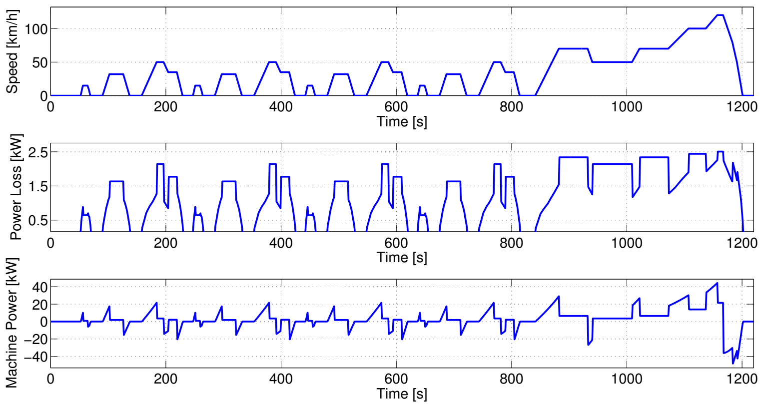

Figure 5.12: *NEDC* cycle speed, power losses and total power in the machine

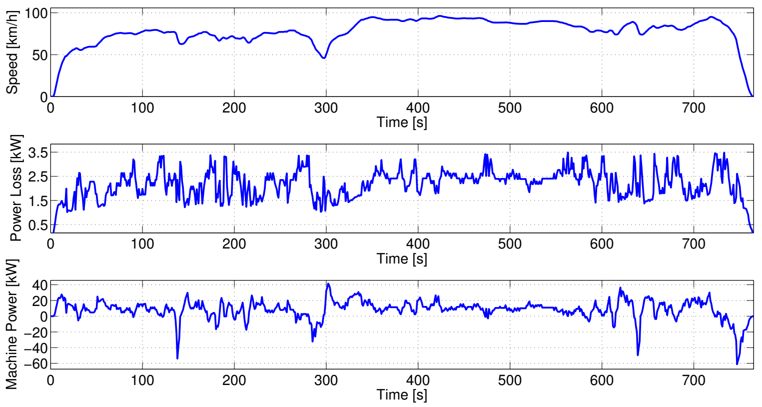

Figure 5.13: *FTP Highway* cycle speed, power losses and total power in the machine

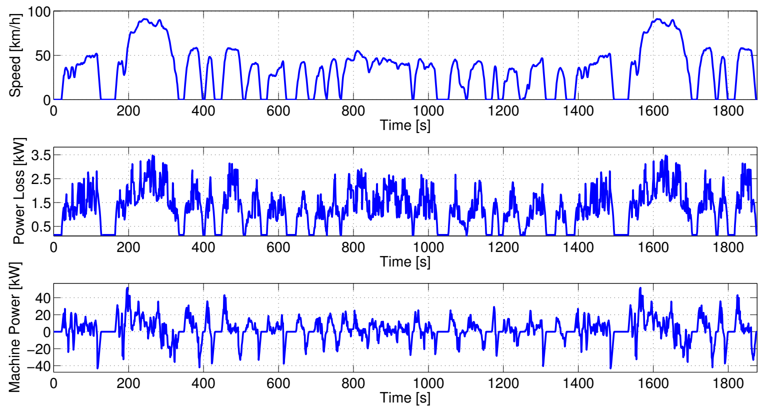

Figure 5.14: *FTP-75* cycle speed, power losses and total power in the machine

it is 83.1% for *NEDC*, 77.8% for *FTP Highway* and 81.8% for *FTP-75*. As expected, a highway driving scenario, where regenerative braking is not usual, gives a poorer performance compared to urban *NEDC* or *FTP-75*.

The maximum magnitude of total electric drive loss is found to be 2.5kW in case of *NEDC* and 3.5kW in *FTP Highway* and *FTP-75*. The maximum propulsion power is 42kW in *NEDC*, 40kW in *FTP Highway* and 55kW in *FTP-75*. On the other hand, the maximum regenerated power is 46kW in *NEDC*, 60kW in *FTP Highway* and 43kW in *FTP-75*.

These maximum regeneration values are not in accordance with the cycle efficiency, as the *FTP Highway* has the highest regeneration magnitude but the worst overall efficiency. This is caused by the regeneration frequency to be smaller than in case of *NEDC* and *FTP-75*. This conclusion is consistent with the general belief that the electric vehicles have the greatest impact in urban environments, in contrast with interurban performances, where regenerative breaking is not a key asset.

6

Harmonic analysis of forces and torques and NVH evaluation

6.1 Time transient analysis

In order to evaluate potential NVH issues, time or frequency domain FEM studies must be carried out. The torque waveforms in one steady state complete revolution are shown in figure 6.1, where an average torque of around $53.2Nm$ and a torque ripple of around 4% are extracted at $9575rpm$, 1% slip. When evaluating the frequency decomposition of these variables, see lower plot in figure 6.1, it is found that in this case study, all torque ripple FFT coefficients are under $0.5Nm$ between 0 and $12kHz$. From this frequency on, the ripple is assumed to not be transmitted to the drivetrain, due to the bigger time constant the mechanical system has with respect to the electrical system.

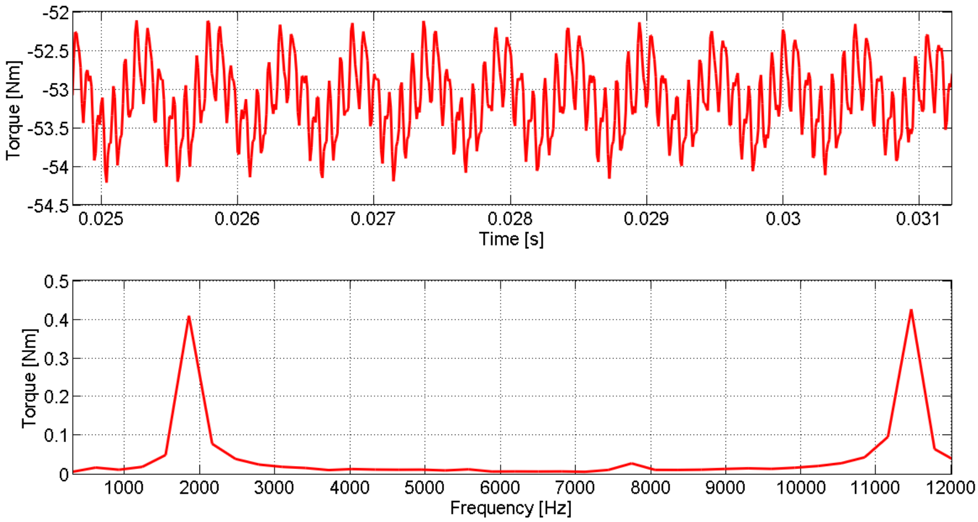

Figure 6.1: Steady state time dependent torque characteristic of the motor. Upper, time dependent torque; lower, FFT of torque excluding $0th$ harmonic

The forces on the stator teeth, however, have a different behavior than that of the torque. As displayed on figures 6.2c and 6.3c, this variable has a much more fluctuating value. It can be extracted from 6.2d and 6.3d that the harmonic orders of the forces are not the same as in case of the torque.

What is more, it is already expected from section 2.3.1 that forces have a different frequency spectrum than that of the magnetic flux density, as they are a squared function of B, and this certainly changes the frequency spectrum of the resulting magnitude, see appendix A.2.

Apart from this, results correlate with what theory predicts in term of harmonic orders, see section 2.3.1. Figure 6.2 shows the time and frequency domain plots of magnetic flux density and radial Maxwell forces in the center of the stator tooth surface. Harmonics for radial and tangential components of the magnetic flux density can be found on orders 18, 20, 37 and 39, see figures 6.2b and 6.3b. Forces can be found on orders 2, 17, 19, 21, 36, 38 and 40, due to these being in orders 0, 2, $n \pm 1$ and $2n$, where n is any magnetic flux density harmonic.

If the stator tooth corner point is selected, on the same surface between stator and air gap, it is seen this point experiences the greatest magnetic flux density in the whole machine, a bigger tangential magnitude can be expected in both magnetic flux density and Maxwell force. It can be seen in figures 6.3a and 6.3b that the tangential component is bigger compared to the point in the tooth center, in figures 6.2a and 6.2b. As far as the Maxwell forces are concerned, this phenomenon is also given. The corner point suffers from a much greater tangential stress, shown in figures 6.3c and 6.3d, compared to the center point, in figure 6.2c and 6.2d.

6.2 Campbell diagrams

Figures 6.4a, 6.5a and 6.6a show the Campbell diagram of the torque ripple, and the most important excitations happen in the $6th$ and $36th$ harmonic. On the other hand, the force excitations, which can be seen in figures 6.4b, 6.5b and 6.6b, take place in the $2nd$, $17th$, $19th$, $21th$, $36th$, $38th$ and $40th$.

The $0th$, $2th$, $17th$, $19th$, $21th$, $36th$, $38th$ and $40th$ are present in all cases , as theory predicts in section 2.3.1, and can be compared with the potential Campbell diagram form figure 4.12. Saturation appears as $6th$ order in the torque ripple, as predicted in 2.3.2. Orders $42th$ and $48th$ appear as torque harmonics in the case of 3% slip. Orders $17th$, $19th$, $21th$ and $24th$ appear as torque harmonics in the case of eccentricity and 3% slip. On the other hand, there are no alterations in the orders of force harmonics.

As saturation is seen as a potential source of harmonics, it must be thoroughly controlled. Even such small values of saturated area as those of table 6.1 cause noticeable torque excitations. The material BH-curve can be seen in figure 4.2a.

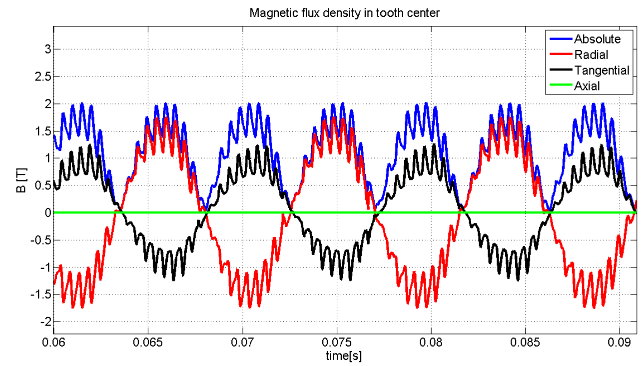

(a) B: Time domain

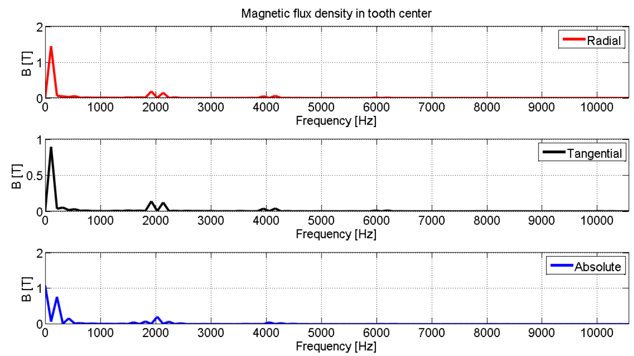

(b) B: Frequency domain

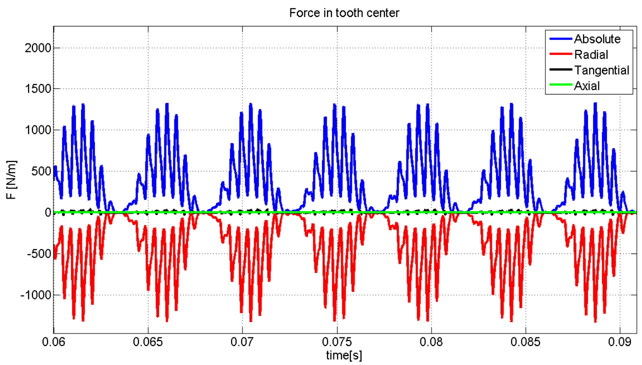

(c) Force: Time domain

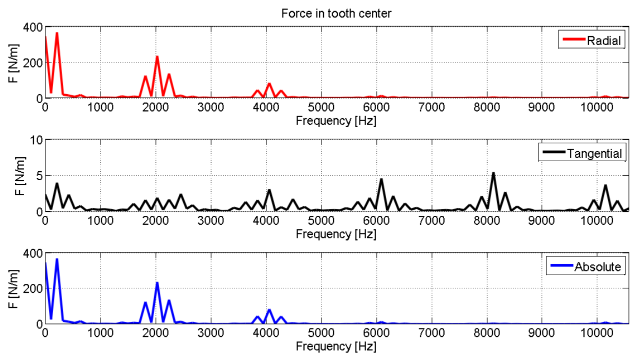

(d) Force: Frequency domain

Figure 6.2: Magnetic flux density and forces plot in tooth surface center point for 3% slip at $110Hz$ supply, $3201rpm$

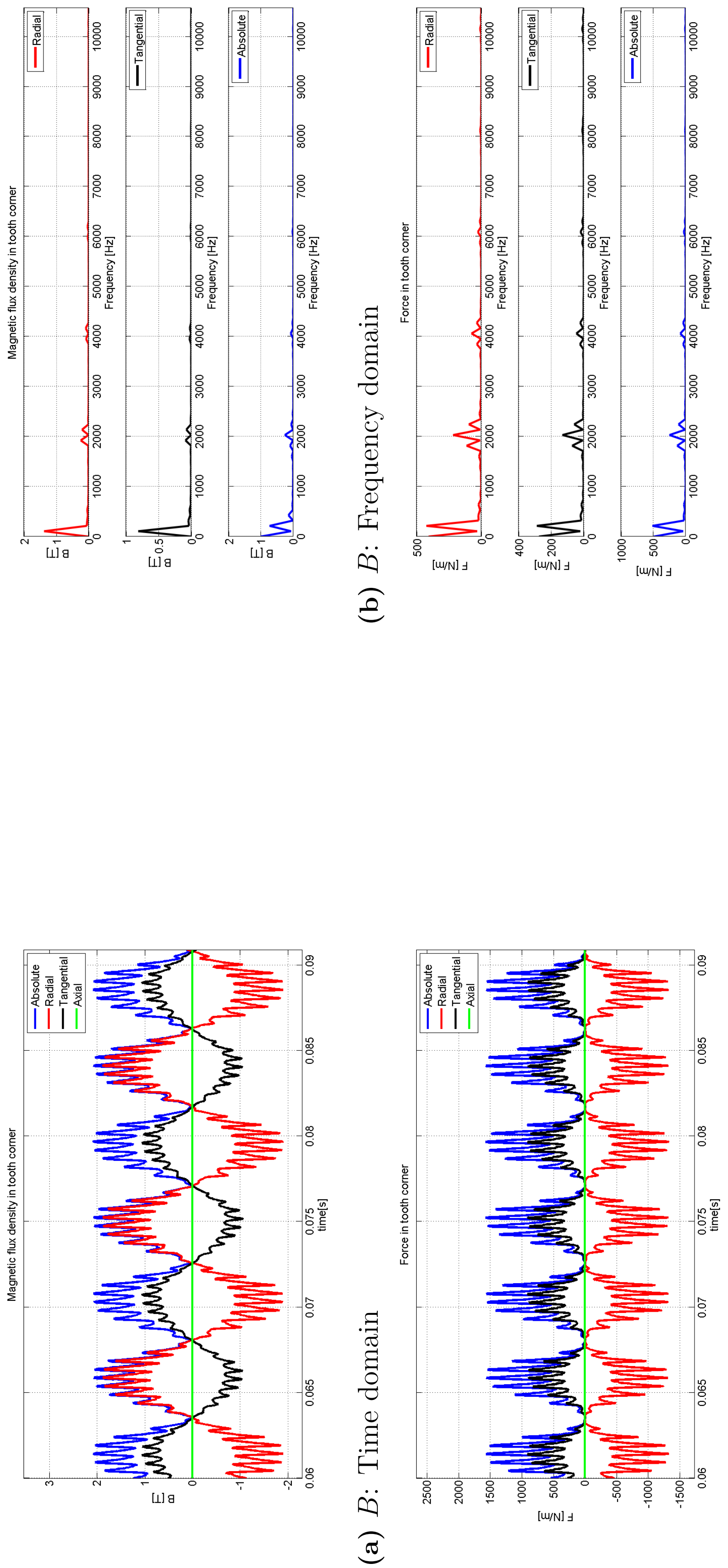

(a) B: Time domain

(b) B: Frequency domain

(c) Force: Time domain

(d) Force: Frequency domain

Figure 6.3: Magnetic flux density and forces plot in tooth surface corner point for 3% slip at 110Hz supply, 3201rpm

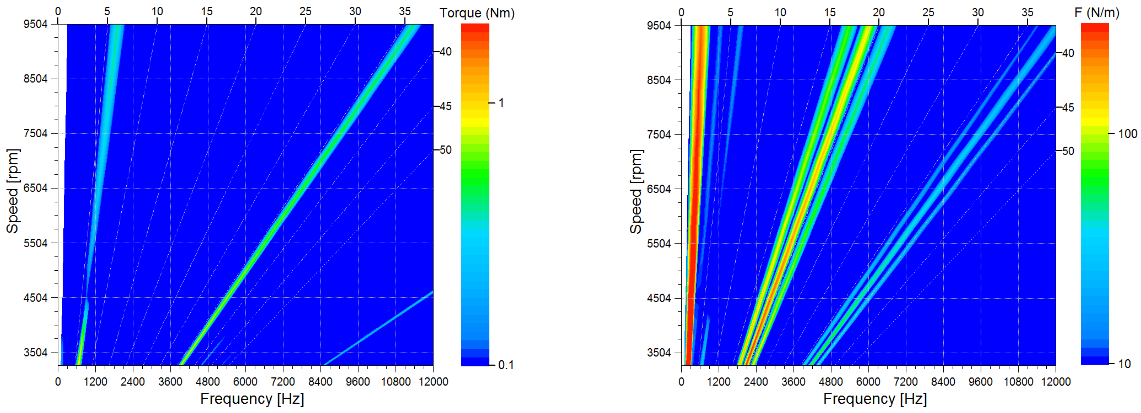

(a) Torque (b) Forces

Figure 6.4: Campbell diagram with 1% slip

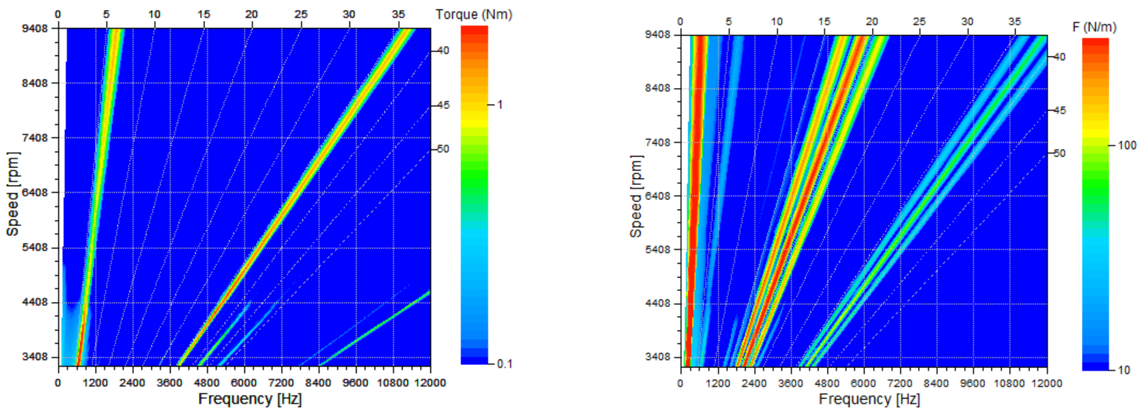

(a) Torque (b) Forces

Figure 6.5: Campbell diagram with 2% slip

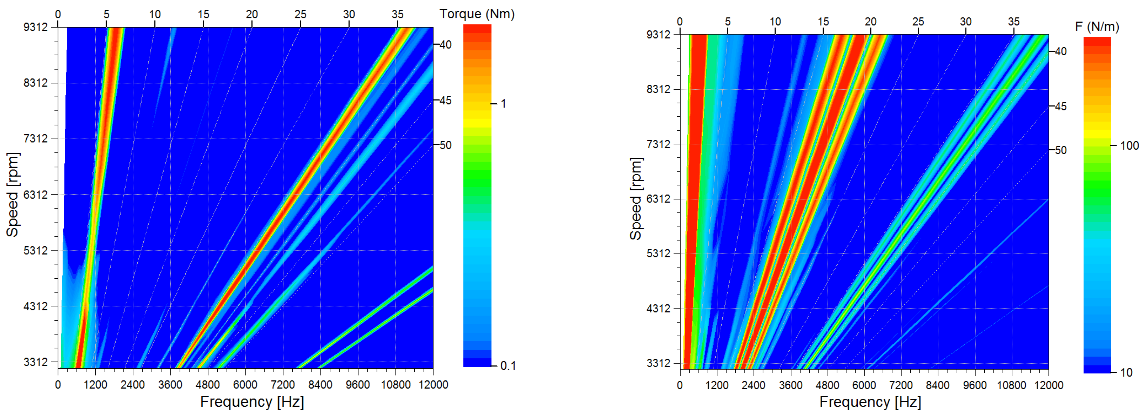

(a) Torque (b) Forces

Figure 6.6: Campbell diagram with 3% slip

Table 6.1: Saturated area computation at $200Hz$ supply frequency and 3% slip

Threshold B $[T]$	Area above threshold [%]
2.2	0.001
2	0.0126
1.8	0.094
1.6	1.42
1.4	3.46
1.2	9.44

6.3 Modal Analysis

For the calculation of the potentially harmful operations points, a modal analysis or mechanical resonance analysis is performed with *NASTRAN* software. Although there have been researchers focusing only on the stator housing [55], this approach is not accurate enough for a full drivetrain evaluation [56, 57]. Therefore, a full driveline modal analysis is performed [46], even though only the stator shapes are shown in figure 6.7, for the sake of simplicity. In these figures, the scale is not relevant, since it does not take the actual forces into account, and thus, only virtual representation of relative displacement is shown.

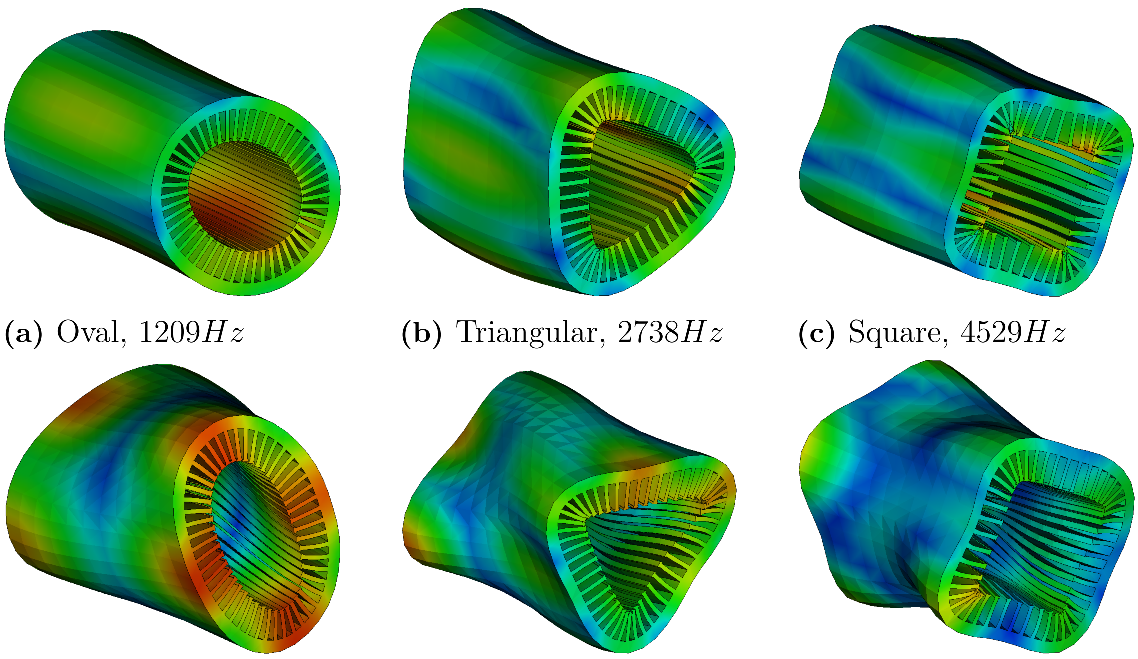

(a) Oval, $1209Hz$ **(b)** Triangular, $2738Hz$ **(c)** Square, $4529Hz$

(d) Oval, $2140Hz$ **(e)** Triangular, $3589Hz$ **(f)** Square, $5361Hz$

Figure 6.7: Modal shapes of the stator. Courtesy of Gergő Gömöri [46].

In any case, it is important to note that there are many more mode shapes than those where the stator gets excited to its natural frequencies. Figure 6.8 illustrates two examples, the first being at $3379Hz$, without stator resonance, and the second at $4529Hz$, representing the full drivetrain virtual displacement from figure 6.7c, where the stator is excited at its resonance frequency. As every element has several natural frequencies, all of them have to be studied in order to numerically assess the noise and/or vibration the driveline will cause.

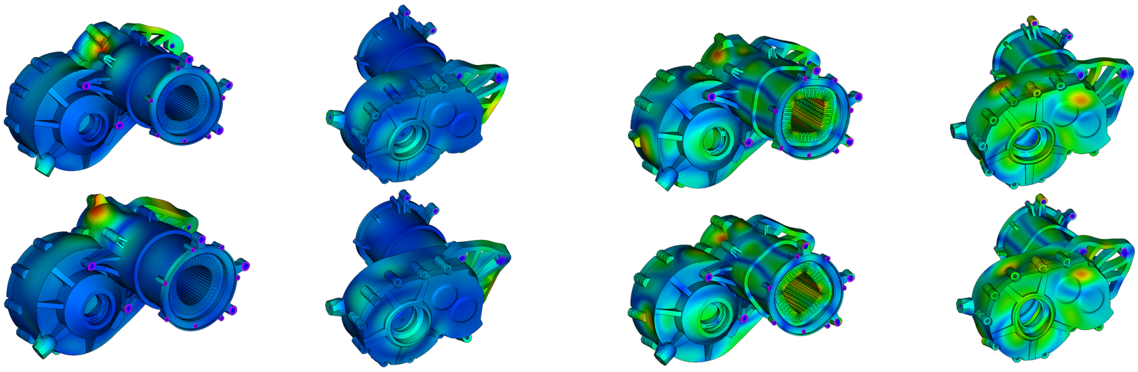

(a) $3379Hz$ **(b)** $4529Hz$

Figure 6.8: Modal shapes of the full drivetrain housing. Courtesy of Gergő Gömöri [46].

6.4 Interaction between Modal Analysis and Campbell diagrams

As mentioned in section 4.4, one of the main reasons to use Campbell diagrams is that mechanical resonances can be easily predicted and detected by means of this representation. To evaluate this, the natural or resonance frequencies from figure 6.7 are represented as vertical lines. Then, crossings of torque and force harmonics with these vertical lines are marked with circles, as in figures 6.9 and 6.10. It is important to note that these vertical lines are found on resonance frequencies of the stator only, but, as mentioned in the previous section, there are numerous natural frequencies for each component, and all of them must be studied.

Horizontal lines are drawn where the marked circles are found. In this manner, the potentially dangerous operation speeds are obtained. Then, forces and torque ripple at this speed are computed with *NASTRAN* and *AVL Excite*, in order to obtain the surface velocity or displacement caused by the excitations and amplified by resonances.

The results for the separate analyses are displayed on figure 6.11, 6.11a for torque ripple and gearbox, and 6.11b in case of Maxwell forces. The scale is maintained in both, so that it can be easily seen that electromagnetic forces applied on the stator cause a much greater impact, with maximum levels of $106.7dB$ compared to $92.3dB$ from torque, on the *NVH* assessment of this specific electric drive.

Then, both studies are coupled and the total resulting surface velocities calculated.

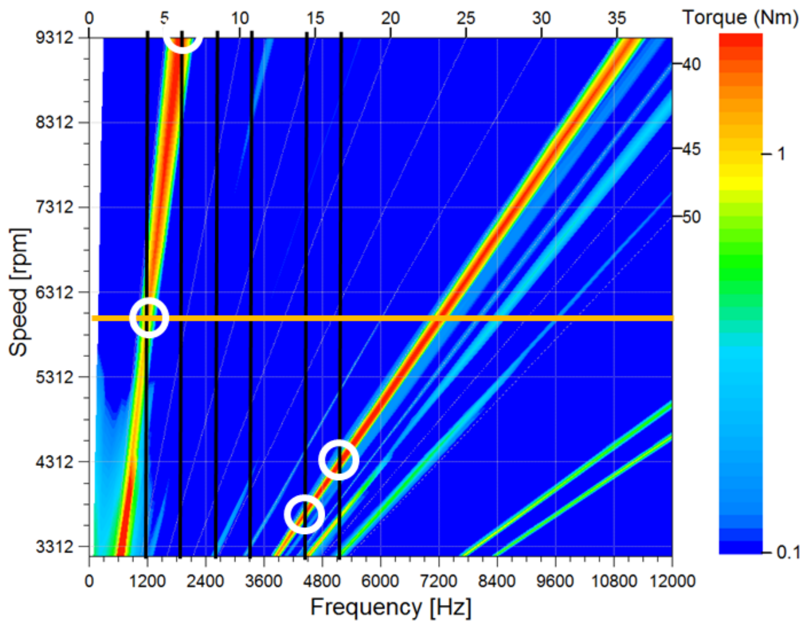

Figure 6.9: Torque Campbell diagram with resonance frequencies as vertical lines and operation speed as horizontal line

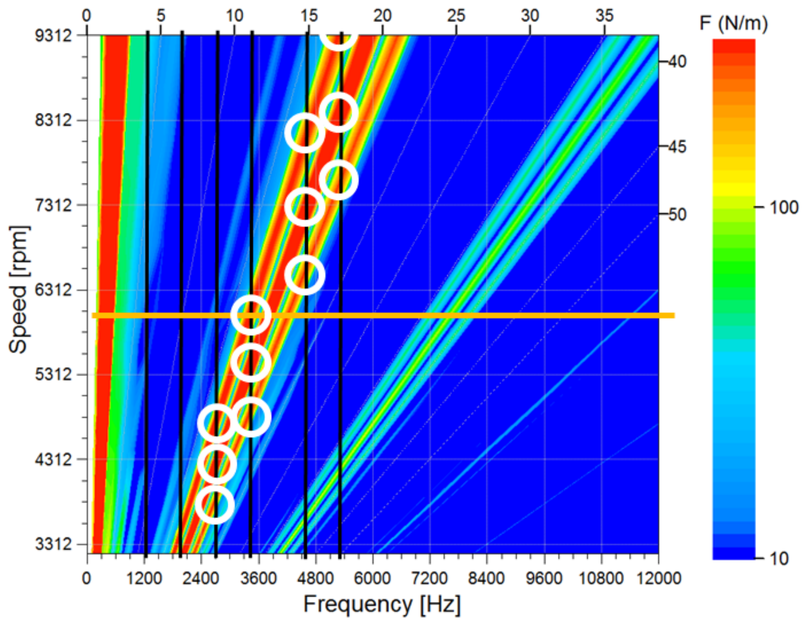

Figure 6.10: Force Campbell diagram with resonance frequencies as vertical lines and operation speed as horizontal line

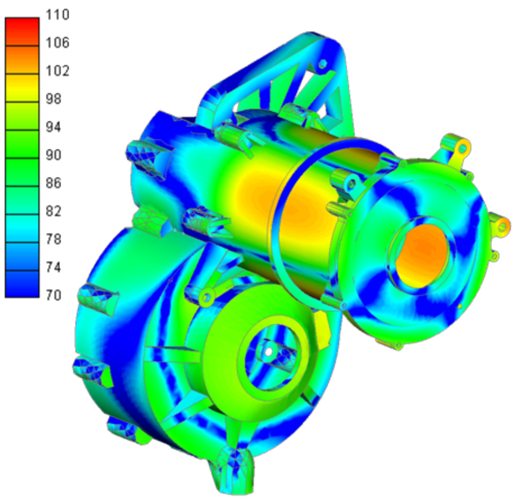

(a) Mechanical

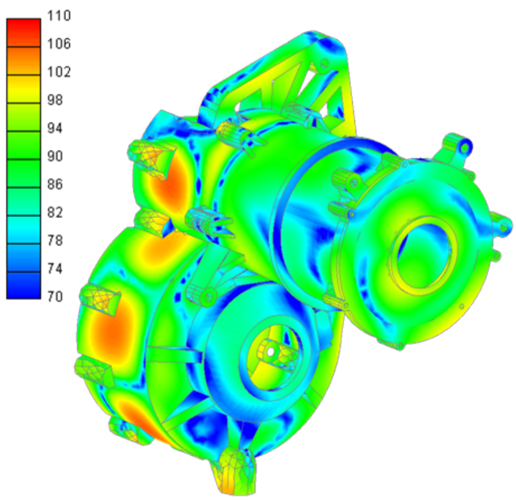

(b) Electromagnetic

Figure 6.11: Response to separate excitations in the drivetrain at $3429Hz$, $6045rpm$. Courtesy of Gergő Gömöri [46].

The output of this coupling can be seen in figure 6.12. The scale is kept equal to the one from figure 6.11, but the combined analysis gives a maximum of $108.3dB$. As a rule of thumb in the company, levels over $100dB$ are considered harmful. From this evaluation, it is found that the mounts are the main problematic areas. To solve this, either a redesign of these or the machine could be implemented, but it is believed that implicit indications to the controller can avoid potentially harmful operation points, by prioritising NVH performance instead of maximum efficiency in the operation ranges where there are noise or vibration issues.

Even though there are infinite modal shapes, such as those from figure 6.7 or 6.8, excitation in electrical machines only happen in full rotation harmonics, and, therefore, the frequencies which are not integer harmonics do not need to be studied.

Another example of these integer harmonic excitation can be found in figure 6.13. This frequency takes the vibration to a magnitude of $116.2dB$. However, in this case the maximum amplitude of the normal surface velocity is given around the stator housing, which could lead to displacement in the structure of the machine. These could act as a source of eccentricity, as the stator would be displaced with respect to the motion region of the drive. This could create local saturation where the air gap becomes smaller than rated, leading to new harmonic orders in torque and force excitations or additional heat losses.

6.5 Eccentricity analysis

In order to simulate manufacturing tolerances or shaft bending due to clearances in bearings and stiffer gear contact vibration, a shaft plus rotor dynamic eccentric-

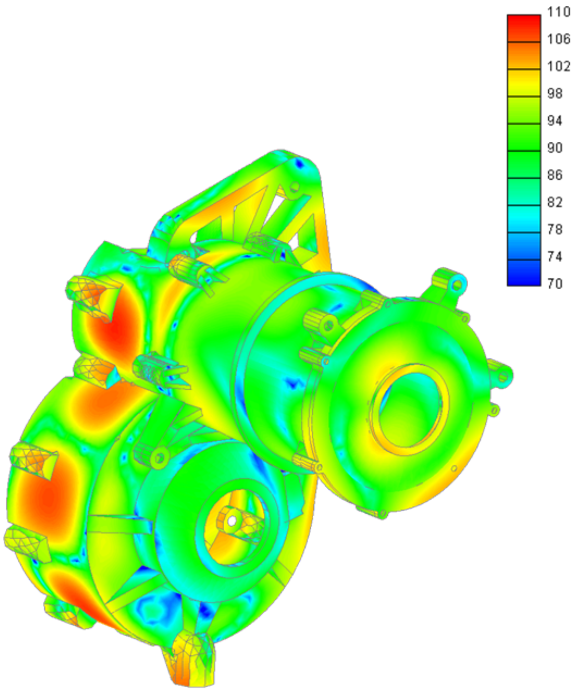

Figure 6.12: Surface normal velocities due to combined excitation at $3429Hz$, $6045rpm$

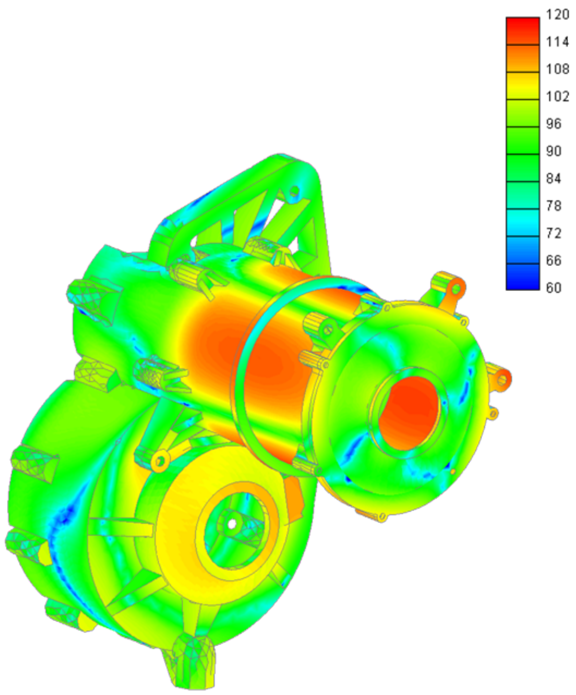

Figure 6.13: Surface normal velocities due to combined excitation at $1209Hz$, $6045rpm$

ity analysis is carried out. An excessive eccentricity can lead to additional noise radiation or even structural failure of the system. However, relevant experts in the company suggest that 15 micrometers (1.8% of the gap) might be a realistic maximum value for this analysis due to the bending and stiffness of the shaft.

Using the value of 15 um eccentricity as an example allows the processing of new Campbell diagrams, in figures 6.14a and 6.14b. It is seen that the forces do not suffer from a substantial alteration, since magnitudes in the most important orders, $2nd$, $17th$, $19th$ and $21st$, are reduced, but new orders do not appear. The ratio of forces with $15\mu m$ divided by the non-eccentric case can be seen in figure 6.15b. At low speeds, eccentricity affects the different orders in a very distinct manner, *i.e.* order 2 is reduced by less than 3%, whereas order 17 decreases by 15%. At higher speed, the change is more uniform for all orders, between 9 and 11%.

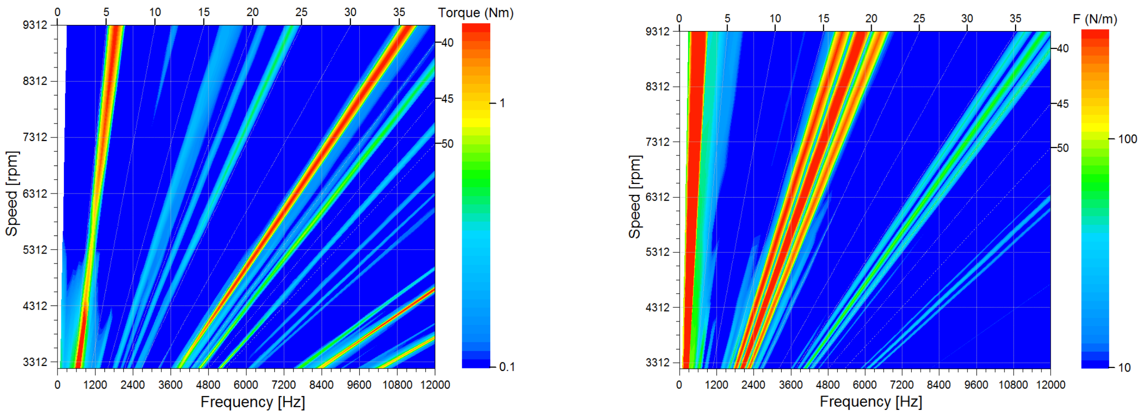

(a) Torque **(b)** Forces

Figure 6.14: Campbell diagram with 3% slip and $15\mu m$ dynamic eccentricity

This implies a very strong non-linear behavior. Apart from this, many new torque ripple orders, such as $17th$, $19th$, $21th$ and $24th$, appear in the torque Campbell diagram, see figure 6.14a. On the other hand, the ratio of torques with $15\mu m$ divided by the non-eccentric case can be seen in figure 6.15a. At low speeds, order 6 is increased by 10%, whereas order 36 is reduced by 55%. At high speeds, order 6 decreases by 7% and order 36 increases by 35%.

6.6 Harmonic order and slip correlation

If a predictive model of excitations was to be built, the first approach should be to see the correlation between the load, or slip, and the resultant torque and force harmonic spectrum. Therefore, the Campbell diagrams in figures 6.4, 6.5 and 6.6 should be analyzed. The *AVL IMPRESS Chart* tool has the capability to analyze the magnitude variation for each harmonic order along the full speed range, a functionality which is found to be very useful for finding correlations between different slips and torque and force harmonics. This could also help predict the effect of

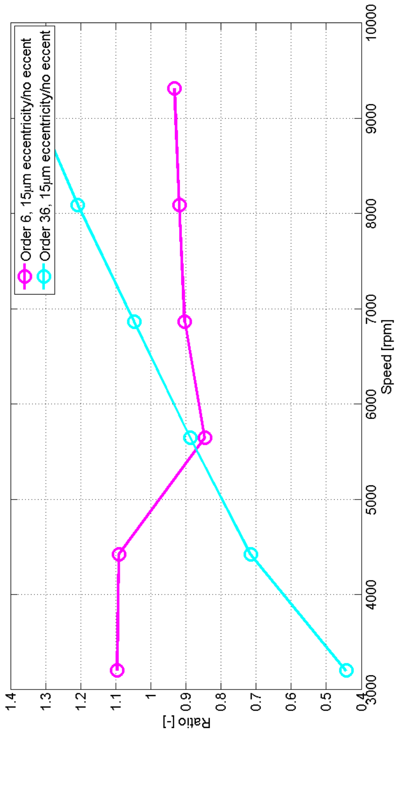

(a) Torque

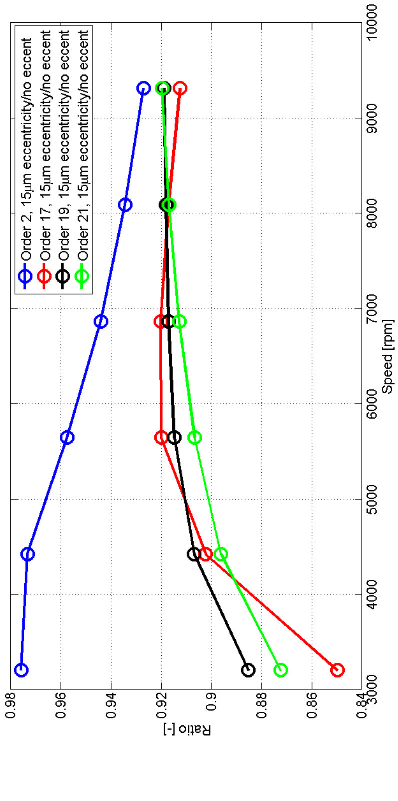

(b) Force

Figure 6.15: Ratio of harmonics with 15 μm dynamic eccentricity divided by the non-eccentric case

manufacturing tolerances, such as eccentricity in figure 6.14.

The $6th$ and $36th$ torque harmonic orders can be seen in figure 6.16. The correlation between slips and harmonic excitation magnitudes is clearly non-linear, as in the eccentricity case. This is caused by the non-linearity of the stator and rotor core materials.

The $6th$ order 1% slip case varies between maximum $0.99Nm$ $3267rpm$ and minimum $0.13Nm$ at $4514rpm$, with a mean value of $0.42Nm$. The 2% slip case keeps the maximum at $3234rpm$, with a magnitude of $2.92Nm$, whereas the minimum, $0.81Nm$, is found at $5704rpm$, with a mean value of $1.38Nm$. A further increase in the load to 3% makes the maximum magnitude reach $4.28Nm$ at $3201rpm$, the minimum stays at $1.14Nm$ $5645rpm$ and the average is $2.20Nm$. Introducing 15 micrometers dynamic eccentricity causes the average to decrease to $2.17Nm$, with maximum $4.69Nm$ at $3201rpm$ and minimum $0.96Nm$ at $5645rpm$.

The $36th$ order 1% slip case has a minimum of $0.41Nm$ at $9504rpm$ and maximum $0.86Nm$ $3267rpm$, with a mean value of $0.63Nm$. Increasing the load to 2% slip moves the maximum to $4469rpm$, with a magnitude of $1.89Nm$, whereas the minimum, $1.18Nm$, is also found at the highest speed, $9408rpm$, averaging $1.43Nm$. The 3% case makes the maximum magnitude reach $2.93Nm$ at $4423rpm$, the minimum is $1.58Nm$ at $3201rpm$ and the average is $2.15Nm$. 15 micrometers dynamic eccentricity cause the average to decrease to $2.01Nm$, with maximum $2.43Nm$ at $9312rpm$ and minimum $0.70Nm$ at $3201rpm$.

As far as the Maxwell forces are concerned, these are, again, strongly non-linear, but, generally, decrease as speed increases. Figure 6.17 shows the speed and slip dependency of force orders $2nd$, $17th$, $19th$ and $21st$.

The $2nd$ order 1% slip case has maximum $857.2N/m$ $3267rpm$ and a minimum of $243.3N/m$ at $9504rpm$, with a mean value of $468.91N/m$. Increasing the slip to 2% keeps the maximum at the lowest speed, $3234rpm$, with a magnitude of $1088N/m$, whereas the minimum, $355.6N/m$, is found at $9408rpm$, averaging $619.07N/m$. The 3% case makes the maximum magnitude reach $1681N/m$ at $3201rpm$, the minimum is $877.5N/m$ at $9312rpm$ and the average is $1174.7N/m$. 15 micrometers dynamic eccentricity cause a variation of the average, a decrease to $1123.2N/m$, with maximum $1640N/m$ at $3201rpm$ and minimum $813.5N/m$ at $9312rpm$.

The $17th$ order 1% slip case has a minimum of $77.81N/m$ at $9504rpm$ and maximum $174.9N/m$ $3267rpm$, with a mean value of $119.3N/m$. Analogously to the $2nd$ order, increasing the slip to 2% keeps keeps the maximum at the lowest speed, $3234rpm$, with a magnitude of $284.1N/m$, whereas the minimum, $165N/m$, is found at $9408rpm$, averaging $223.21N/m$. However, the 3% case makes the maximum magnitude reach $409.1N/m$ at $4423rpm$, the minimum is $319.1N/m$ at $9312rpm$ and the average is $364.94N/m$. 15 micrometers dynamic eccentricity reduce the force magnitudes, taking the average to $329.46N/m$, with maximum $369.2N/m$ at $4423rpm$ and minimum $291.2N/m$ at $9312rpm$.

The 19*th* order follows the same behavioral pattern as the 17*th*, *i.e.* 1% slip case has a minimum of 126.4N/m at 9504rpm and maximum 299.5N/m 3267rpm, with a mean value of 195.48N/m. Increasing the slip to 2% keeps keeps the maximum at the lowest speed, 3234rpm, with a magnitude of 493.2N/m, whereas the minimum, 281.9N/m, is found at 9408rpm, averaging 375.8N/m. The 3% case makes the maximum magnitude reach 702.3N/m at 4423rpm, the minimum is 543.6N/m at 9312rpm and the average is 625.87N/m. 15 micrometers dynamic eccentricity cause the average to decrease to 569.11N/m, with maximum 636.9N/m at 4423rpm and minimum 499.5N/m at 9312rpm.

The 21*st* order follows the trends from order 2, with a decrease in the magnitude of the force as speed increases. 1% slip case has a minimum of 51.28N/m at 9504rpm and maximum 135.2N/m 3267rpm, with a mean value of 81.04N/m. Increasing the slip to 2% keeps keeps the maximum at the lowest speed, 3234rpm, with a magnitude of 234.2N/m, whereas the minimum, 130.4N/m, is found at 9408rpm, averaging 160.8N/m. The 3% case makes the maximum magnitude reach 311N/m at 3201rpm, the minimum is 270.6N/m at 9312rpm and the average is 288.21N/m. 15 micrometers dynamic eccentricity cause the average to decrease to 260.36N/m, with maximum 271.3N/m at 3201rpm and minimum 248.9N/m at 9312rpm.

The general conclusion for induction machine driven automotive drivetrains is that a greater slip implies bigger excitations, both in the form of torque ripple or stator forces. At the same time, it is seen that the introduction of 15 micrometer eccentricity alters force magnitudes on the stator in all significant orders, but increases magnitudes of several torque harmonic orders.

6.7 Integral evaluation of normal surface velocity levels

If the resulting vibrations from the torque ripple and force mapping analyses are combined together in the frequency domain, a sound simulation can be carried out. The *AVL Excite* software is used to perform the normal surface velocity integral.

The outcome of this operation can be seen in figure 6.18, where the torque ripple only, forces only and the combined evaluations are displayed separately. This allows the engineer to discriminate the different noise sources and correct the excessive values by efficiently focusing on the mechanical or electromagnetic origin of them.

It can be seen that the combined radiation has maximums over 100dB in 1.2kHz, with 110.8dB, 2.3kHz, with 100.2dB, and 4.4kHz, with 108.1dB. The dominant source at 1.2 kHz and 4.4kHz is the electromagnetic force, whereas the torque ripple governs the combined magnitude at 2.3kHz. This can help tackle the *NVH* issue more efficiently by accurately analysing the nature of the vibration.

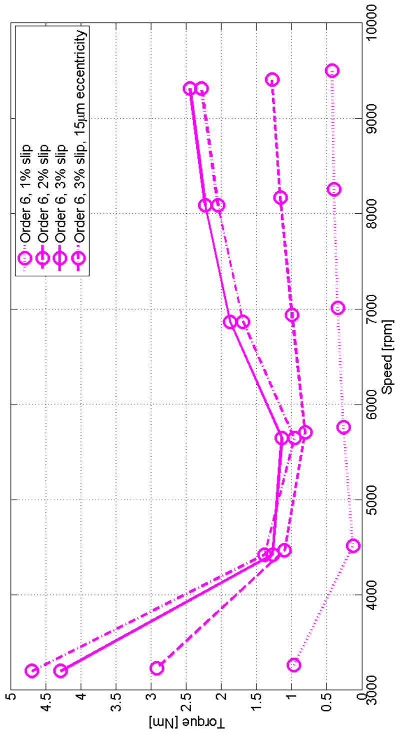

(a) Order 6

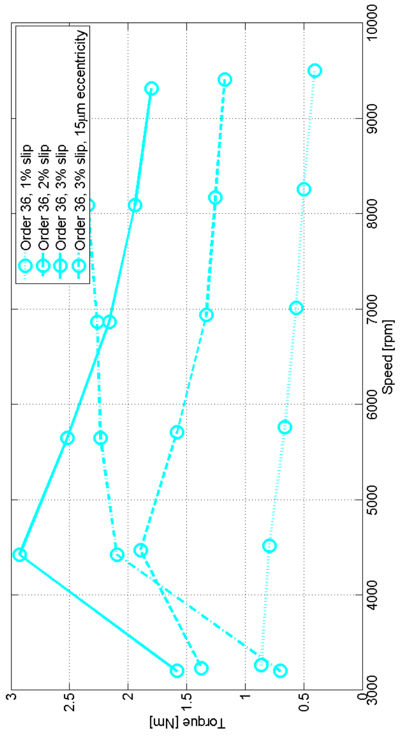

(b) Order 36

Figure 6.16: Most important torque harmonic magnitudes depending on slips, speeds and existence of eccentricity

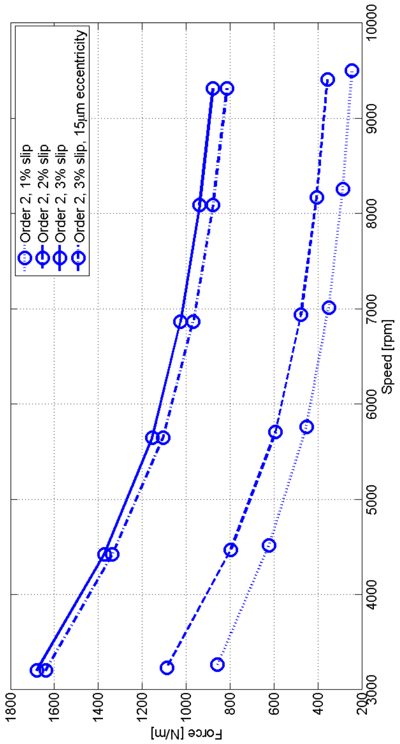

(a) Order 2

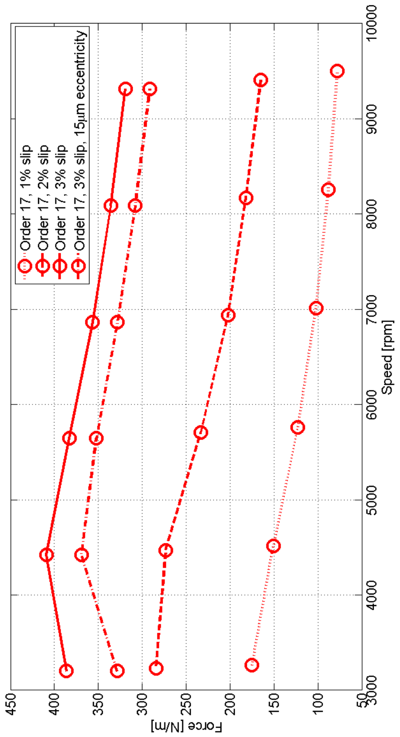

(b) Order 17

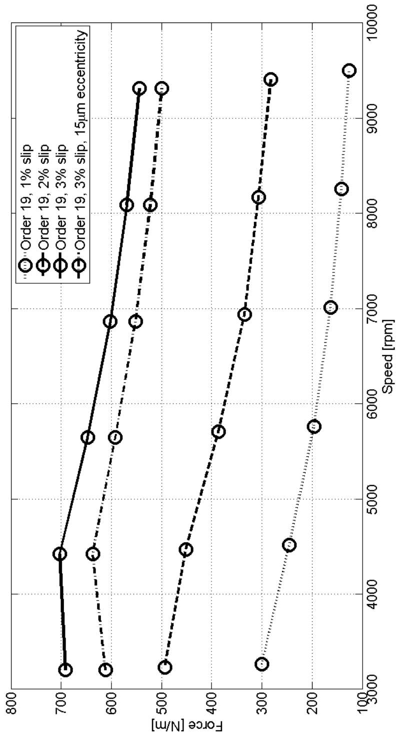

(c) Order 19

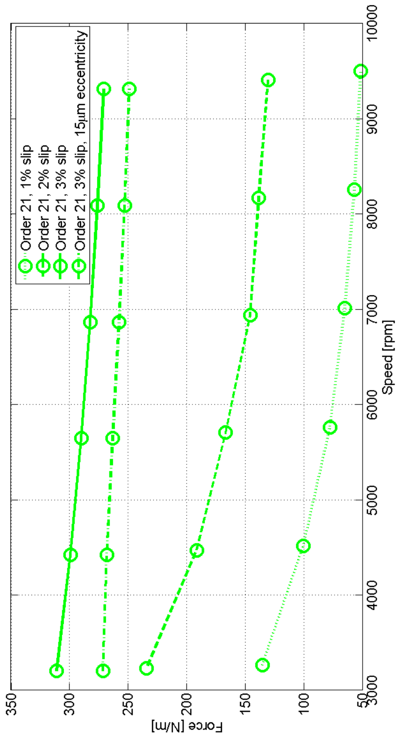

(d) Order 21

Figure 6.17: Most important force harmonic magnitudes depending on slips, speeds and existence of eccentricity

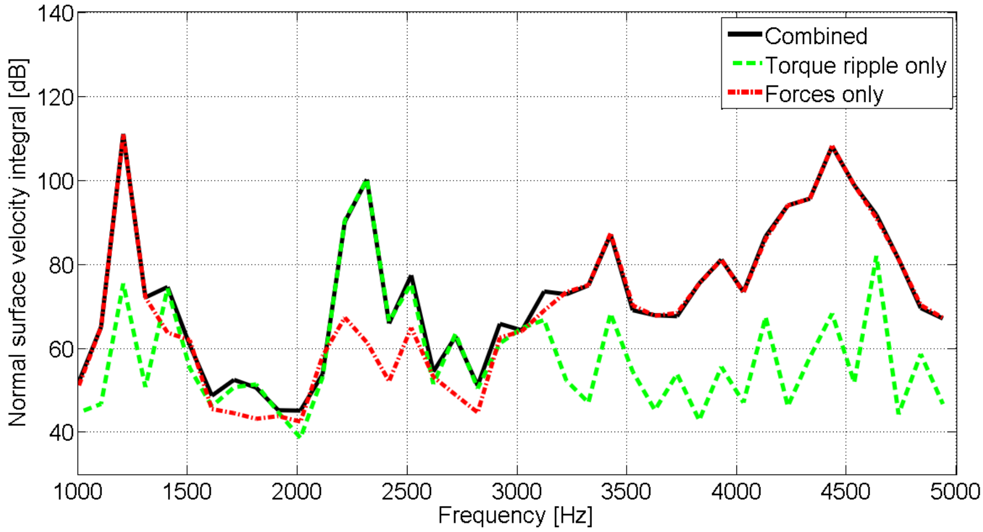

Figure 6.18: Surface normal velocity integral due to combined excitation at 6045rpm 3% slip

7

Conclusion and future work

7.1 Conclusion

This project has studied the design of an electric drive powering an automotive drivetrain and the generated harmonic excitations in form of torque ripple or forces on the stator. The designed induction machine was aimed to evaluate *NVH* issues in fully electric or hybrid drivetrains.

The whole drivetrain is considered in the structural analysis study, which is necessary, instead of considering only the stator. The additional components increase the mass, area and volume of the studied structure, parameters which change the mechanical resonance frequencies interacting with the harmonic excitations created by the machine.

The theoretical models for prediction of harmonic orders are found to correlate with the resulting *FEM* harmonic orders, even though these do not predict the excitation magnitude. Potential force harmonics are found in orders 0, 2 and $n \pm 1$.

It is seen that a low-torque-ripple design aim might not be enough for reducing the *NVH* issues, and specially radiated noise, in a fully electric or hybrid drivetrain, since Maxwell forces experienced by the stator can be present in frequencies where there is no torque harmonic.

The machine geometry greatly influences the harmonic content of the torque and forces. Analytic models are not used in this thesis to evaluate the harmonic content magnitude, but useful guidelines can be made for computation of potentially harmful operation points. However, *FEM* simulations are needed in order to create thorough Campbell diagrams and get the magnitudes of torque and force excitations.

Campbell diagrams reflect that harmonic excitation is non-linearly dependent on the slip and speed, as the core material has a non-linear behavior, due to the non-linear BH-curve, which leads to saturation.

Generated force excitations depend on the geometrical situation of the studied point. The tooth corner undergoes stress from both tangential and radial forces, whereas the tooth center has only stress of radial nature.

Force and torque excitations are only found on integer harmonic orders, with mechanical rotation frequency as base for these.

The interaction between Campbell diagrams and mechanical resonance frequencies from modal analysis is accurate and simple. Forces are mapped on the stator in frequency domain, whereas torque ripple is applied in time domain in order to obtain the frequency response of the gearbox and shafts. These frequency domain excitations are applied on the drivetrain and surface velocity levels are obtained as *NVH* key performance indicator.

Eccentricity alters radial forces, non-linearly, for most relevant harmonic orders. However, new orders appear in torque ripple, and $36th$ order in torque is increased at high speeds.

Analysis of the normal surface velocity integral can lead to a more efficient approach to *NVH* problem solving, by discriminating the source of the noise radiation.

7.2 Future work

In order to get a more thorough evaluation of the *NVH* characteristics of a fully electric or hybrid driveline, the effect of power electronics should be included. These could amplify or reduce the existing excitations either as torque or as force harmonics.

The interaction of mechanical, electrical and thermal interfaces has not been fully attained, as thermal analysis was out of the scope of this thesis. However, this should be ideally included in the machine assessment, as it is a crucial aspect and the major limitation with regard to operation range limits.

Regarding eccentricity, manufacturing tolerances were studied, but magnetostriction was not. It is believed that the optimization of the machine and drivetrain would require an effort in the study of magnetic deformations and their impact on heat transfer and *NVH*.

Bibliography

[1] M Jozwicka and T Pulles. Identifying transport's potential contributions to future GHG reduction. *European Commision Directorate-General Environment*, 2009.

[2] I Skinner, H van Essen, R Smokers, and N Hill. Towards the decarbonisation of the EU's transport sector by 2050. *European Commision Directorate-General Environment*, 2010.

[3] Stephen J. Chapman. *Electric Machinery Fundamentals*. McGraw-Hill, 4th edition, 2005.

[4] Zhi Yang, Fei Shang, I P Brown, and M Krishnamurthy. Comparative Study of Interior Permanent Magnet, Induction, and Switched Reluctance Motor Drives for EV and HEV Applications. *IEEE Transactions on Transportation Electrification*, 1(3):245–254, oct 2015.

[5] I Boldea, L N Tutelea, L Parsa, and D Dorrell. Automotive Electric Propulsion Systems With Reduced or No Permanent Magnets: An Overview. *IEEE Transactions on Industrial Electronics*, 61(10):5696–5711, oct 2014.

[6] Jean Le Besnerais. *Réduction du bruit d'origine magnétique dans une machine asynchrone alimentée par MLI - règles de conception silencieuse et optimisation multi-objectif*. PhD thesis, École Centrale de Lille.

[7] A. Belahcen. *Magnetoelasticity, Magnetic Forces and Magnetostriction in Electrical Machines*. PhD thesis, Helsinki University of Technology, Helsinki, Finland, 2004.

[8] Xiaoping Tu, Louis A. Dessaint, Roger Champagne, and Kamal Al-Haddad. Transient modeling of squirrel-cage induction machine considering air-gap flux saturation harmonics. *IEEE Transactions on Industrial Electronics*, 55(7):2798–2809, 2008.

[9] Austin Hughes and Bill Drury. *Electric Motors and Drives*. Elsevier Ltd., 2006.

[10] Dulce F Pires, V Fernão Pires, J F Martins, and A J Pires. Rotor cage fault diagnosis in three-phase induction motors based on a current and virtual flux approach. *Energy Conversion and Management*, 50(4):1026–1032, 2009.

[11] J Herbst, J Hahne, H Jordan, H Liu, A Gattozzi, and B Wu. Challenges in the design of a 100 kw induction motor for a PHEV application. In *Vehicle Power and Propulsion Conference, 2009. VPPC '09. IEEE*, pages 408–413, sep 2009.

[12] S Li, Y Li, W Choi, and B Sarlioglu. High speed electric machines #x2014; Challenges and design considerations. In *Electrical Machines (ICEM), 2014 International Conference on*, pages 2549–2555, sep 2014.

[13] G Kloos. Magnetostatic Maxwell stresses and magnetostriction. *Electrical Engineering*, 81(2):77–80.

[14] D.J. Griffiths. *Introduction to Electrodynamics*. Prentice Hall, 3rd ed. edition, 1999.

[15] Rathna Kumar Sastry Chitroju. *Improved Performance Characteristics of Induction Machines with Non-Skewed Asymmetrical Rotor Slots*. PhD thesis, Kungliga Tekniska Högskolan, Stockholm, Sweden, 2009.

[16] I Petrov, P Ponomarev, Y Alexandrova, and J Pyrhönen. Unequal Teeth Widths for Torque Ripple Reduction in Permanent Magnet Synchronous Machines With Fractional-Slot Non-Overlapping Windings. *IEEE Transactions on Magnetics*, 51(2):1–9, feb 2015.

[17] Y Plotkin, M Stiebler, and D Hofmeyer. Sixth torque harmonic in PWM inverter-fed induction drives and its compensation. *IEEE Transactions on Industry Applications*, 41(4):1067–1074, 2005.

[18] Juha Pyrhönen, Tapani Jokinen, and Valéria Hrabovcová. *Design of Rotating Electrical Machines*. John Wiley & Sons, Ltd, 2008.

[19] I Boldea and S A Nasar. *The Induction Machine Handbook*. CRC Press LLC, 2009.

[20] K Maliti. *Modelling and analysis of magnetic noise in squirrel-cage induction motors*. PhD thesis, Kungliga Tekniska Högskolan, Stockholm, Sweden, 2000.

[21] JSOL Corporation. JMAG Application Catalog. *JMAG User Support*, 2016.

[22] Lennart Harnefors. *Control of Variable-Speed Drives*. Mälardalen University, Västerås, 2002.

[23] M Popescu. *Induction Motor Modelling for Vector Control Purposes*. Helsinki University of Technology, 2000.

[24] P. Vas. *Parameter Estimation, Condition Monitoring and Diagnosis of Electrical Machines*. Oxford University Press, 1990.

[25] Arnaud Hubert. *Contribution à l'étude des bruits acoustiques generes lors de l'association machines electriques - convertisseurs statiques de puissance. Ap-*

plication a la machine asynchrone. PhD thesis, Université de Technologie de Compiègne, Compiègne, France, 2001.

[26] Ned Mohan, Tore M Undeland, and William P Robbins. *Power Electronics: Converters, Applications and Design*. John Wiley & Sons, Inc., 2003.

[27] Y Miyama, M Hazeyama, S Hanioka, N Watanabe, A Daikoku, and M Inoue. PWM Carrier Harmonic Iron Loss Reduction Technique of Permanent Magnet Motors for Electric Vehicles. *IEEE Transactions on Industry Applications*, PP(99):1, 2016.

[28] Peng Yu, Tong Zhang, and Puhui Liu. NVH Prediction of Electric Vehicle Driving Motor Base on Radial Electromagnetic Force Analysis. *Advanced Materials Research*, 13(1):1537–1540, 2013.

[29] Wei Tong. *Mechanical Design of Electric Motors*. Taylor & Francis Group, LLC, 2014.

[30] Peng Yu, Tong Zhang, and Puhui Liu. NVH Characteristic Prediction of An Electric Vehicle Reducer. pages 1656–1659, 2013.

[31] Jean Le Besnerais, Vincent Lanfranchi, Michel Hecquet, Pascal Brochet, and Guy Friedrich. Acoustic noise of electromagnetic origin in a fractional slot induction machine. *COMPEL, The international journal for computation and mathematics in electrical and electronic engineering*, 27(5):1033–1052, 2008.

[32] T. C. Limt and R. Singh. Vibration transmission through rolling element bearings. Part iii: geared rotor system studies. *Journal of Sound and Vibration*, (M(1)):31–54, 1991.

[33] B Klarin, C Vock, C Nolfe, D De Stefanis, C Cardone, T Pappalardo, C Grasso, S C A Elasis, Carmine Nolfe, Davide De Stefanis, Ciro Cardone, Teresa Pappalardo, and Corrado Grasso. Enhanced Power Unit NVH Simulation with MBD Solver AVL EXCITE. *SAE Technical Paper*, (2005-24-016), 2005.

[34] Z Neusser, Martin Sopouch, Thomas Schaffner, and Hans-herwig Priebsch. Multi-body Dynamics Based Gear Mesh Models for Prediction of Gear Dynamics and Transmission Error. *SAE Technical Paper*, (2010-01-0897), 2010.

[35] M. Brunner, M. Mehrgou, and H. Bansal. Advances in Rattle and Whine simulation. In *CTI Symposium*, Berlin, 2015.

[36] Homayoun Meshgin Kelk and Hamid A Toliyat. Modeling and Analysis of Cage Induction Motors under Rotor Misalignment and Air Gap Eccentricity. In *Industry Applications Conference, 40th IAS Annual Meeting*, volume 3, pages 1324–1328, 2005.

[37] A Ghoggal, S E Zouzou, H Razik, M Sahraoui, and A Khezzar. An improved model of induction motors for diagnosis purposes – Slot skewing effect and air –

gap eccentricity faults. *Energy Conversion and Management*, 50(5):1336–1347, 2009.

[38] M Sahraoui, A Ghoggal, S E Zouzou, and M E Benbouzid. Simulation Modelling Practice and Theory Dynamic eccentricity in squirrel cage induction motors – Simulation and analytical study of its spectral signatures on stator currents. *Simulation Modelling Practice and Theory*, 16(9):1503–1513, 2008.

[39] Jawad Faiz and Mansour Ojaghi. Mechatronics Different indexes for eccentricity faults diagnosis in three-phase squirrel-cage induction motors : A review. *Mechatronics*, 19(1):2–13, 2009.

[40] B M Ebrahimi J Faiz. Magnetic field and vibration monitoring in permanent magnet synchronous motors under eccentricity fault. *IET Electric Power Applications*, 6(December 2010):35–45, 2012.

[41] AVL List Gmbh. AVL Excite theory, 2013.

[42] H.P. Wallin, U. Carlsson, M. Åbom, and H. Bodén. *Sound and vibration*. Stockholm: Institutionen för farkostteknik, Tekniska högskolan, 2010.

[43] J. Y. Wong. *Theory of Ground Vehicles*. John Wiley & Sons, Inc., 4th ed. edition, 2008.

[44] T.D. Gillespie. *Fundamentals of Vehicle Dynamics*. Society of Automotive Engineers Inc., 1992.

[45] Wolf-Heinrich Hucho, editor. *Aerodynamics of Road Vehicles*. Butterworth-Heinemann Ltd, 1987.

[46] G. Gömöri. NVH Analysis of a Fully Electric Drivetrain. Master's thesis, Budapest University of Technology and Economics, Budapest, Hungary, 2016.

[47] W. Campbell. Protection of Steam Turbine Disk Wheels from Axial Vibration. *Transactions of the ASME*, pages 31–160, 1924.

[48] A Ghaderi, T Umeno, and M Sugai. An Altered PWM Scheme for Single-Mode Seamless Control of AC Traction Motors for Electric Drive Vehicles. *IEEE Transactions on Industrial Electronics*, 63(3):1385–1394, 2016.

[49] O Wasynczuk, S D Sudhoff, K A Corzine, J L Tichenor, P C Krause, I G Hansen, and L M Taylor. A maximum torque per ampere control strategy for induction motor drives. *IEEE Transactions on Energy Conversion*, 13(2):163–169, jun 1998.

[50] W Sung, J Shin, and Y s. Jeong. Energy-Efficient and Robust Control for High-Performance Induction Motor Drive With an Application in Electric Vehicles. *IEEE Transactions on Vehicular Technology*, 61(8):3394–3405, oct 2012.

[51] P. Vas. *Vector Control of AC Machines*. Oxford University Press, 1990.

[52] D. W. Novotny and T. A. Lipo. *Vector Control and Dynamics of AC Drives*. Oxford University Press, 1996.

[53] G S Buja and M P Kazmierkowski. Direct torque control of PWM inverter-fed AC motors - a survey. *IEEE Transactions on Industrial Electronics*, 51(4):744–757, 2004.

[54] A Putri, S Rick, D Franck, and K Hameyer. Application of sinusoidal field pole in a permanent magnet synchronous machine to improve the NVH behavior considering the MTPA and MTPV operation area. *IEEE Transactions on Industry Applications*, PP(99):1, 2016.

[55] Jean-Baptiste Dupont, Racha Aydoun, and Pascal Bouvet. Simulation of the Noise Radiated by an Automotive Electric Motor : Influence of the Motor Defects. *SAE Technical Paper*, (2014-01-2070), 2014.

[56] P Humbert, P Pellerey, and S Cristaudo. Electromagnetic and Structural Coupled Simulation to Investigate NVH Behavior of an Electrical Automotive Powertrain. *SAE Technical Paper*, (2012-01-1523):395–404, 2015.

[57] Yuan Fang and Tong Zhang. Modeling and Analysis of Electric Powertrain NVH Under Multi-Source Dynamic Excitation Multi-Excitations. *SAE Technical Paper*, (2014-01-2870), 2015.

A

Appendix

A.1 Transformations

Clarke amplitude invariant simplified transformation

$$\begin{bmatrix} S_\alpha \\ S_\beta \end{bmatrix} = \frac{2}{3} \begin{bmatrix} 1 & -\frac{1}{2} & -\frac{1}{2} \\ 0 & \frac{\sqrt{3}}{2} & -\frac{\sqrt{3}}{2} \end{bmatrix} \begin{bmatrix} S_a \\ S_b \\ S_c \end{bmatrix}, \quad \begin{bmatrix} S_a \\ S_b \\ S_c \end{bmatrix} = \begin{bmatrix} 1 & 0 \\ -\frac{1}{2} & \frac{\sqrt{3}}{2} \\ -\frac{1}{2} & -\frac{\sqrt{3}}{2} \end{bmatrix} \begin{bmatrix} S_\alpha \\ S_\beta \end{bmatrix} \tag{A.1}$$

Park transformation between rotating and stationary coordinate system

$$\underline{u}^s = \underline{u} e^{j\theta},\ \underline{u} = \underline{u}^s e^{-j\theta},\ e^{j\theta} = \cos\theta + j\sin\theta \tag{A.2}$$

$$\begin{bmatrix} u_\alpha \\ u_\beta \end{bmatrix} = \begin{bmatrix} \cos\theta & -\sin\theta \\ \sin\theta & \cos\theta \end{bmatrix} \begin{bmatrix} u_d \\ u_q \end{bmatrix}, \quad \begin{bmatrix} u_d \\ u_q \end{bmatrix} = \begin{bmatrix} \cos\theta & \sin\theta \\ -\sin\theta & \cos\theta \end{bmatrix} \begin{bmatrix} u_\alpha \\ u_\beta \end{bmatrix} \tag{A.3}$$

A.2 Fourier Series

Let f be a piecewise continuous function on $[-\pi, \pi]$. Then the *Fourier* series of f is

$$a_0 + \sum_{n=1}^{\infty} (a_n \cos nx + b_n \sin nx) \tag{A.4}$$

where the coefficients a_0, a_n, and b_n in this series are defined by

$$a_0 = \frac{1}{2\pi} \int_{-\pi}^{\pi} f(x)\, \mathrm{d}x,\ a_n = \frac{1}{\pi} \int_{-\pi}^{\pi} f(x) \cos nx\, \mathrm{d}x,\ b_n = \frac{1}{\pi} \int_{-\pi}^{\pi} f(x) \sin nx\, \mathrm{d}x \tag{A.5}$$

and are called the *Fourier* coefficients of f.

A.3 Motor description

Figures A.1 and A.2 show the slot diagram and design table of the machine, respectively.

The correlation matrix from JMAG Designer can be found in figure A.3, with red as indicator of positive correlation and blue as sign of negative correlation.

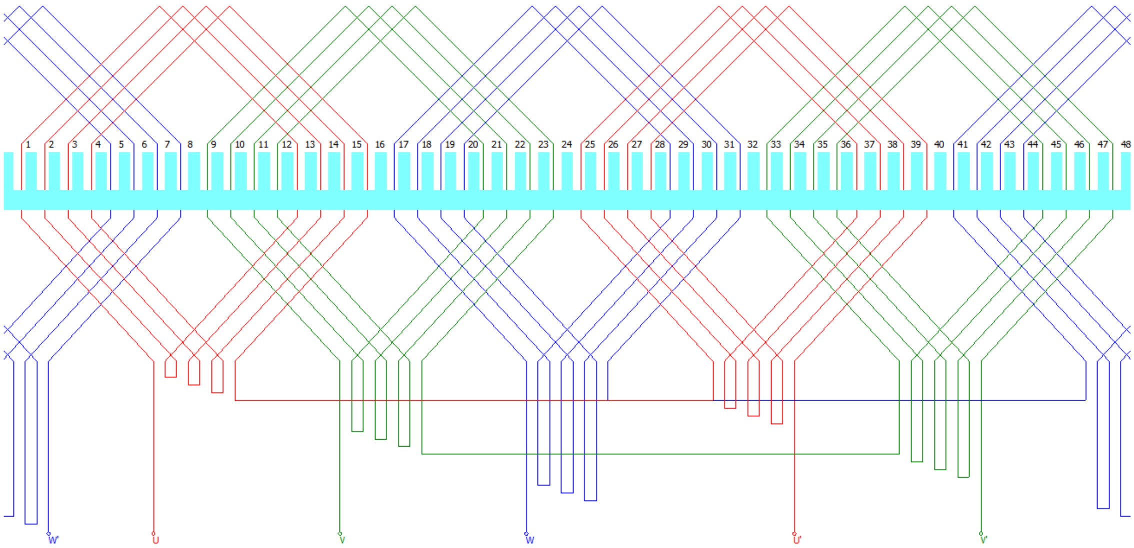

Figure A.1: Slot diagram of the induction motor

Machine Constant		
Revolution Speed	N, rpm	7125
Equivalent Circuit Parameters	Primary leakage reactance, ohm	0.3666
	Secondary leakage reactance, ohm	0.3666
	Primary resistance, ohm	0.01786
	Secondary resistance, ohm	0.1268
	Iron loss equivalent conductance, S	8.101e-03
	Excitation susceptance, S	0.06861
	Exciting Inductance, H	9.279e-03
Starting Characteristics	Starting Impedance (real part), ohm	0.1394
	Starting Impedance(imaginary part), ohm	0.7245
	Starting Current(RMS), A	442.8
	Starting Torque, Nm	90.17
Electric Part	Primary Current(RMS), A	294.1
	Wire Current Density, A/m^2	1.178e+07
Power	Torque, Nm	232.6
	Efficiency, %	91.94
	Power, W	1.735e+05
	Power Factor	0.6549
Loss	Copper Loss, W	1.377e+04
	Iron Loss, W	1446
	1st Current Loss, W	4634
	2nd Current Loss, W	9134
Electric Circuit	Magnetizing Current, A	16.85

Winding	
Connection Type	Star Connection
Series Number	8
Parallel Number	1
Number of Turns	4
Setting Type	Round Wire Dimension
Wire Diameter, mm	0.85
Film Thickness, mm	0.041
Number of Strands	44
Insulation Thickness, mm	0
Slot Fill Factor, %	50.01
Max Slot Fill Factor, %	55
Correction Factor	1
Slot Area, mm^2	240.1
Conductor Area, mm^2	2.27
Phase Resistance, ohm	0.01786
Winding	Auto Winding
Number of Layers	1
Coil Pitch	12
Coil Current Density(@1A), A/mm^2	0.04005

Drive	
Phase Voltage(Amp), V	462
Frequency, Hz	250

Dimension		
All	Outer Diameter, mm	250
	Gap Length, mm	0.85
	Thickness, mm	290
	Number of Poles	4
stator : so_000	Number of Slots	48
	Outside Diameter, mm	250
	Inside Diameter, mm	145.5
	Tooth Width, mm	5.208
	Slot Opening Width, mm	2.6
	Core Back Width, mm	15
	Tooth Tang Depth, mm	2.554
im_rotor : rim_002	Number of Secondary Conductor	38
	Outside Diameter, mm	143.8
	Shaft Diameter, mm	40
	Bar Outer Side Radius, mm	2.2
	Bar Inner Side Radius, mm	1.6
	Bar Outer Center Depth, mm	2.5
	Distance between Bar Edge Centers, mm	23
	Slot Opening Width, mm	3
	Teeth Top R, mm	0.4
End Ring	Section Type	Trapezoid
	Height, mm	5.031
	Upper Width, mm	15.09
	Lower Width, mm	15.09
	Offset, mm	0
	Effective Section Area, %	100
	Resistance, ohm	1.205e-04

Mass Property		
Total	Total Weight, kg	113.5
	Total Volume, mm^3	1.457e+07
Stator	Coil - Mass, kg	38.18
	Coil - Volume, mm^3	4.262e+06
	Stator Core - Mass, kg	46.94
	Stator Core - Volume, mm^3	5.979e+06
	Part Weight(so_000)	85.12
Rotor	Cage - Mass, kg	2.946
	Cage - Volume, mm^3	1.092e+06
	Rotor Core - Mass, kg	25.41
	Rotor Core - Volume, mm^3	3.237e+06
	Part Weight(rim_002)	28.36
Inertia, kg m^2	Cage	0.01039
	Rotor Core	0.06411
	Total	0.0745

Materials		
Coil	Category	Copper
	Density, kg/m^3	8960
	Drive Temperature, degC	20
	Base Temperature, degC	20
	Temperature Correction Factor, ppm/degC	3810
Stator Core	Category	JFE_Steel - JN_Core
	Type	50JN1300
	Density, kg/m^3	7850
Cage	Category	Aluminium
	Conductivity, 1/(ohm*m)	4e+07
	Density, kg/m^3	2699
Rotor Core	Category	JFE_Steel - JN_Core
	Type	50JN1300
	Density, kg/m^3	7850
Common Material Properties	Iron Loss Correction Factor	1

Figure A.2: Design table of the induction motor

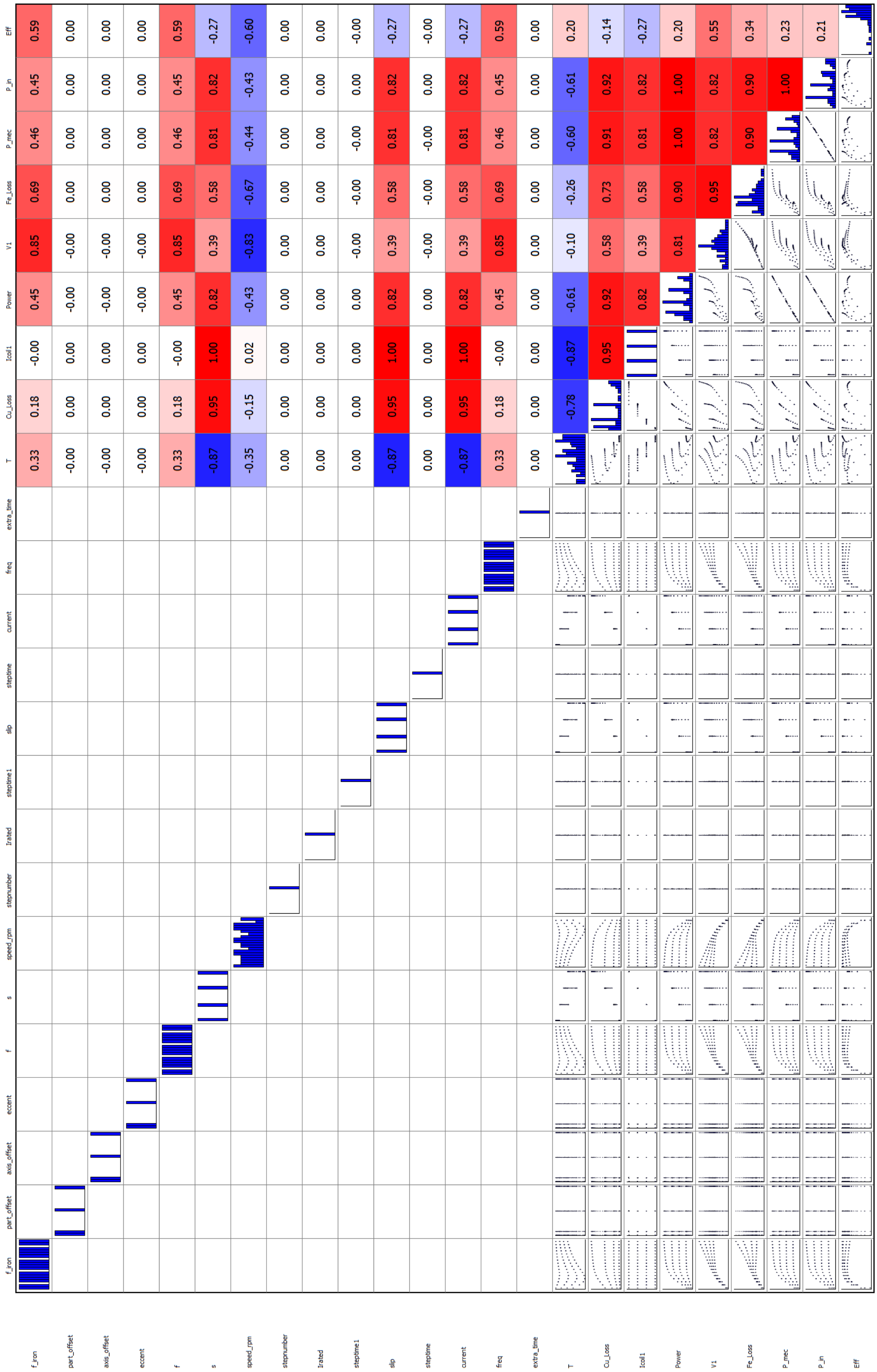

Figure A.3: Correlation matrix of proposed motor design